April 2014

Methods of Engine Degradation Assessment in the Time-Scale Domain

Jeffrey Charles Simmons
University of Massachusetts - Amherst

METHODS OF ENGINE DEGRADATION ASSESSMENT IN THE TIME-SCALE DOMAIN

A Dissertation Presented

by

JEFFREY C. SIMMONS

Submitted to the Graduate School of the
University of Massachusetts Amherst in partial fulfillment
of the requirements for the degree of

DOCTOR OF PHILOSOPHY

February 2014

Mechanical and Industrial Engineering

METHODS OF ENGINE DEGRADATION ASSESSMENT IN THE TIME-SCALE DOMAIN

A Dissertation Presented

by

JEFFREY C. SIMMONS

Approved as to style and content by:

Dr. Kourosh Danai, Chair

Dr. Yossi Chait, Member

Dr. Christopher V. Hollot, Member

Dr. Robert E. LaBarre, Member

Dr. Donald Fisher, Department Head
Mechanical and Industrial Engineering

ACKNOWLEDGMENTS

I would like to thank my academic advisor, Prof. Kourosh Danai, for the expert guidance he provided and his ability to keep me on-track. I could not wish for a better advisor. I would also like to express my appreciation to my committee members, Prof. Christopher Hollot, Prof. Yossi Chait and Dr. Robert LaBarre for the time they devoted to reading and providing insightful feedback on both the thesis proposal and dissertation. Also, I'd like to thank my Pratt & Whitney technical supervision, G. William Gallops, Kathleen Norkevek and Scott Sanicki, for endorsing my PhD. study and obtaining the necessary approval from our supervision as well as their continued support. I also appreciate the effort of Edward A. Marino, also from Pratt & Whitney, who compiled the gas-turbine simulation and created the simulation interface used in this thesis. Finally, I would like to thank my wife, Inge, for her encouragement, support and patience during this journey. I am deeply indebted to all of them.

ABSTRACT

METHODS OF ENGINE DEGRADATION ASSESSMENT IN THE TIME-SCALE DOMAIN

FEBRUARY 2014

JEFFREY C. SIMMONS

B.A. Central Connecticut State University 1995,

M.A. Central Connecticut State University 1998,

Ph.D., UNIVERSITY OF MASSACHUSETTS AMHERST

Directed by: Professor Dr. Kourosh Danai

This dissertation addresses health monitoring of aircraft engines. Two methods are offered for engine degradation assessment: (1) a direct method to isolate degradation of engine components in-flight, and (2) an inverse method to quantify the level of degradations post-flight. The noted feature of the degradation isolation method is its independence from training, which makes it suitable for on-board implementation. The degradation quantification method, on the other hand, is a multi-output method of parameter estimation with the advantage of leveraging the shape attributes of model outputs. The representation of the shape attributes of the various time series, by continuous wavelet transforms (CWTs), is the salient feature of both the direct and inverse methods developed in this research. It enables the isolation of regions in the time-scale plane, called "signatures," wherein the wavelet coefficients of a given transform time series dominate the wavelet coefficients of

the others. These methods of engine degradation isolation and quantification have been validated numerically using the transient outputs of a high-bypass turbo-fan engine model provided by Pratt & Whitney Company.

In the direct method, residuals will continually be formed in-flight to represent the difference between individual outputs and their baseline. These residuals will then be contrasted with each other to reveal "degradation signatures," denoting the effect of the present degradation on individual residuals. To perform degradation isolation, the observed degradation effect will be compared with the pre-established effect of individual components' degradation on the outputs according to the engine model. These pre-established effects are defined according to the sensitivity of outputs to component parameters, denoted as "output/parameter signatures," and to combined component parameters, denoted as "output/component signatures." The effectiveness of the proposed method is evaluated in engine simulations. The results indicate that with the suite of outputs currently available on-board 70% to 96% of the degraded components simulated can be isolated for new and older engines.

In the inverse method, parameter signatures are extracted to denote the regions of the time-scale domain wherein individual output parameter sensitivities are dominant. Justified by this dominance, the prediction error can be attributed in these regions to the error of the corresponding model parameter. This enables parameter estimation to be performed on a small set of wavelet coefficients. These isolated regions of the time-scale plane also reveal numerous transparencies and degrees of freedom to be exploited for parameter estimation. The transparencies include the quality measures of the parameter signatures. The degrees of freedom entail the various shape attributes of outputs that can be included through different wavelet transforms, selectiveness of regions of the parameter signatures that are closest to the edge points (modulus maxima), among others. It is shown that by taking advantage of these transparencies and degrees of freedom, the robustness of

parameter estimation can be improved. The results also indicate the potential for improved precision and faster convergence of the parameter estimates when shape attributes are used in place of the magnitude. Although the inverse method has proven effective in several platforms, it is found to be less effective than nonlinear least squares in application to the engine model, due to the lack of distinction between its output sensitivities.

TABLE OF CONTENTS

LIST OF TABLES

Table **Page**

LIST OF FIGURES

Figure **Page**

INTRODUCTION

Performance of aircraft gas turbine engines deteriorate with age due to corrosion, erosion, and fouling of blades and vanes and increased seal leakages. The customary approach to engine maintenance is to perform regularly scheduled overhauls of engines to restore their performance. But this approach is only suitable for normal engine deterioration: it falls short when components degrade prematurely due to events that potentially degrade cooling flow or increase erosion of compressor blades. Examples of such events are flying through sand storms or volcanic plumes, ice ingestion and blockages to the cooling system due to contaminations. This dissertation introduces a direct method of component degradation isolation that can be readily implemented on-board as a safeguard against accelerated component degradations. Also introduced is a complementary method of component degradation quantification which can operate post-flight to determine the severity of the degradation incurred. In the direct approach, *Damage Signature Isolation Method (DSIM)* [34], which is based on pattern recognition, the effects of component degradations on the outputs are identified first. These effects are then contrasted for component isolation with the characteristic signatures of individual components on the outputs. The traditional impediment to the development of direct solutions for engine health monitoring has been their demand for training to determine the component characteristic signatures; e.g., [16, 17, 36]. The first contribution of this dissertation is to introduce a direct solution that overcomes this traditional barrier. It achieves this by relying on continuous wavelet transforms to both represent and delineate the shape attributes of time signals and the sensitivities of engine outputs to the health parameters.

There are two features of continuous wavelet transforms that are particularly appealing to both the proposed direct and inverse solutions. One is the multi-scale differential feature of these transforms, which enables characterization of the shapes of time signals, as size is quantified in the time domain. The other is their capacity to delineate time signals, which is used for change detection and parameter estimation by isolating regions of considerable deviation in the time-scale domain among the time signals, coined as *signatures*. These signatures offer significant advantages in system identification areas. This dissertation extends their applicability in performance monitoring of gas turbine engines [3, 25–27]. Specifically, the signatures can be used for signal change detection. By using this change detection strategy, the proposed degradation isolation method identifies the unique effects of degradations on the individual outputs as well as the effects of health parameters and components on the output sensitivities. The contrast between the degradation effects and the characteristic effects of parameters and components on the outputs has been shown to provide a considerable level of accuracy for degradation isolation of engine components.

In contrast to the direct approach, the "health parameters" representing the efficiency and flow capacity of individual engine components are estimated in the inverse approach [35]. Parameter estimation is generally performed post-flight using the recorded measurements [4, 5]. Practical considerations often demand in-flight measurements to be acquired during steady-state operation of the engine [10, 11, 21], although the estimation methods, such as the Kalman filter or nonlinear least-squares, would perform more efficiently with transient measurements. With steady-state measurements and in the absence of a priori information about component degradation correlation (e.g., health parameter covariance matrix in [4]), the information content of each measurement is confined to a static gain, therefore, at least as many measurements are needed as the number of parameters to be estimated. Transient measurements, on the other hand, provide more identifiability to the health parameters [7, 9], therefore, they demand fewer sensors [26]. Regardless of the type of mea-

surement used, the inverse approach is iterative and would require the influence coefficient matrix (i.e., Jacobian) at the current parameter estimates. With steady-state measurements, the influence matrix can be obtained a priori to reduce computation [4, 5]. With transient measurements, however, such a priori provision is impossible and function calls (i.e., engine simulations) are necessary, which add to the computation. The use of transient data is rare in currently used diagnostic methods but its use has been previously attempted; Merrington [28, 29] utilized transient data in engine fault diagnosis however, computer limitations at the time, hampered results. The inverse approach is also constrained by the convergence requirements of rich excitation of the outputs and convexity of the error surface [20], which deter its implementation on-board. It is recalled here that databases of pre-generated state-space models such as STORM [8] and eSTORM [13] exist to avoid simulation runs on-board. However, the precision of these models have proven inadequate for on-board parameter estimation.

The contribution to this thesis to the inverse method of degradation quantification is to include the shape attributes of outputs. The current inverse methods rely on the magnitude of the gradient (Jacobian) and of the prediction error. This thesis offers the alternative of using the shape attributes of these entities instead. For application to the jet engine, this thesis extends the capabilities of PARSIM [3] to multiple outputs and wavelet transforms. The salient feature of the proposed method is its size mitigation of the CWT surfaces by focusing on isolated information-rich regions of these surfaces. These regions of the time-scale plane, called 'parameter signatures', can be isolated because of the enhanced delineation of time series in the time-scale domain. Each region is sought wherein the sensitivity of an output to a model parameter dominates its sensitivities to all the other model parameters, hence making it possible to attribute the prediction error to the error of individual model parameters in their corresponding parameter signature [3]. These single-parameter approximations of the prediction error enable, in turn, consideration of

isolated segments of surfaces of the output sensitivities and prediction error for parameter estimation, thus making it tractable to include isolated portions of the CWTs for parameter estimation. A potential pitfall of the above scheme is the absence of parameter signatures due to parameter non-identifiability. For such cases, an alternative integration routine is considered wherein separate estimates of individual model parameters are obtained for their iterative adaptation.

CHAPTER 1

THE GENERAL APPROACH

This dissertation consists of two separate yet complementary parts. The first part (chapter 3) describes the direct method to isolate components of the gas-turbine engine in which the presence of degradation has been detected. The second part (chapter 4) handles the inverse method in which the severity of the component degradation is assessed. The salient feature of the proposed approaches is that it transforms transient time series into a surface in the time-scale domain via continuous wavelet transforms. The two important features of CWTs is their characterization of shape attributes and their delineation of the time series. The hallmark of this approach is its reliance on "signatures" which denote the regions in the time-scale domain of significant deviation between the surfaces. These signatures have been used in this research for signal change detection as well as parameter estimation.

DSIM uses continuous wavelet transforms (CWTs) to represent various shape attributes of outputs/residuals as the basis for identifying the outputs affected by component degradation. It also takes advantage of the enhanced delineation of these wavelet transforms to identify the residuals that are affected by engine degradation as well as to define the influence matrix that associates these residuals with the engine components. The continuous wavelet transforms will be described first then the features that benefit performance monitoring and parameter estimation will be illustrated.

1.1 Transformation to the Time-Scale domain

Briefly, a continuous wavelet transform (CWT) is obtained by the convolution of a wavelet function $\psi_s(t)$ with the signal $f(t)$ [22], as

$$W\{f\}(t,s) = f * \psi_s(t) = \int_{-\infty}^{\infty} f(\tau)\psi_s(t-\tau)d\tau \tag{1.1}$$

where $\psi_s(t) = \frac{1}{s}\psi(\frac{t}{s})$ represents the wavelet function, and t and s denote the translation (time) and dilation (scale) parameters, respectively. The wavelet function can be manipulated in two ways, as shown in Fig. 1.1: (i) it can be moved sideways (translated) to coincide with different segments of the signal, and (ii) it can be widened (dilated) or narrowed (constricted) to align with a larger or smaller segment of the signal at its current location (current time). Dilation in wavelet transforms is analogous to widening or narrowing of the sinusoidal function in the Fourier transform due to the frequency, as such scale, s, in CWT is often paralleled to frequency, hence the name "time-frequency" domain.

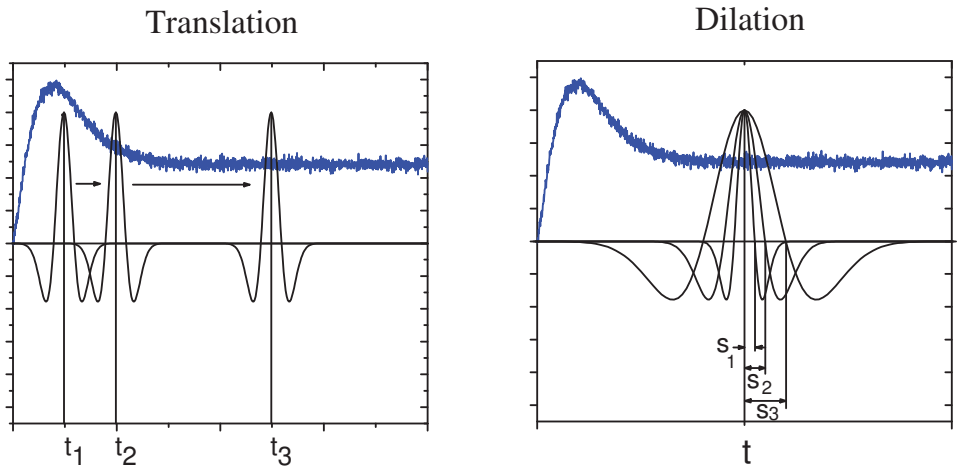

Figure 1.1. Translation and dilation of the Sombrero wavelet across a time signal

For a view of the CWT which is of significance to this research let us consider the CWT of a time signal $f(t)$ at a particular coordinate (t_1, s_1):

$$W\{f\}(t_1, s_1) = \int_{-\infty}^{\infty} f(\tau)\frac{1}{s_1}\psi\left(\frac{t_1 - \tau}{s_1}\right) d\tau \tag{1.2}$$

The wavelet coefficient, $W\{f\}(t_1, s_1)$, which represents the cross-correlation of $f(t)$ with $\psi_{s_1}(t_1)$, depends upon the magnitude of $f(t)$ as well as the conformity of $f(t)$ with the shape of the dilated $\psi_{s_1}(t_1)$. As such, the wavelet coefficients can accentuate minute differences between time signals at the lower scales, when a narrow $\psi_s(t)$ captures the conformity of the wavelet function with a small segment of the time signal [26].

Numerically, the computation of CWTs is significantly facilitated for dyadic time data, similar to fast Fourier transforms. In this dissertation, 128 data points of each time data and 72 scales obtained for the CWTs, result in a time-scale plane of 128 $\times$ 72 pixels with each pixel having unity time and scale dimensions.

1.2 Characterization of Shape Attributes

The capacity to represent the shape attributes of time series is rooted in CWTs' multi-scale differential feature [22]. Consider the wavelet $\psi(t)$ to be the nth order derivative of the smoothing function $\beta(t)$; i.e.,

$$\psi(t) = (-1)^n \frac{d^n(\beta(t))}{dt^n} \tag{1.3}$$

and the continuous wavelet transform of the time function $f(t)$ defined as

$$W\{f\}(t, s) = f * \psi_s(t) = \int_{-\infty}^{\infty} f(\tau)\frac{1}{\sqrt{s}}\psi^* \frac{(\tau - t)}{s} \mathrm{d}\tau \tag{1.4}$$

where $W\{f\}$ denotes the CWT of the time function $f(t)$, $*$ denotes convolution, ψ^* is the complex conjugate of ψ, $\psi_s(t) = \frac{1}{\sqrt{s}}\psi(\frac{t}{s})$, and t and s denote the time (translation) and scale (dilation or constriction) parameters, respectively. Then according to Mallat and

Hwang [24], this wavelet transform is a multiscale differential operator of the smoothed function $f * \beta_s(t)$ in the time-scale domain; i.e.,

$$W\{f\}(t,s) = s^n \frac{d^n}{dt^n} \left(f * \beta_s(t)\right) \tag{1.5}$$

Using this feature, one can utilize a CWT to represent a certain shape attribute of a time series. For instance, one may consider the smoothing function $\beta(t)$ to be the Gaussian function. In this case, the Gauss wavelet which is the first derivative of the Gaussian function, as shown in the left plot of Fig. 1.2, produces a CWT that represents the slope of the signal $f(t)$ smoothed by the Gaussian function, and orthogonal to it. Similarly, the Sombrero wavelet which is the second derivative of the Gaussian function, as shown in the right plot of Fig. 1.2, produces a CWT that denotes the rate of slope change of this smoothed signal in the time-scale domain.

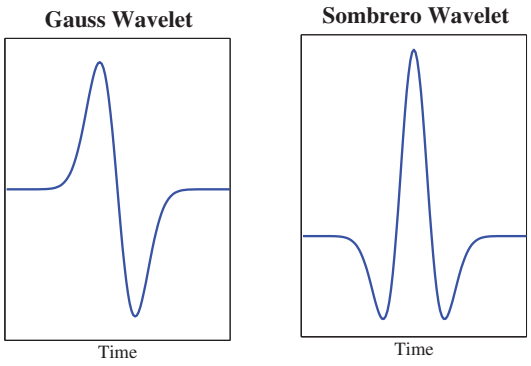

Figure 1.2. Gauss wavelet (left) and Sombrero wavelet (right) which are the first and second derivatives of the Gaussian function, respectively

The shape representation capacity of CWTs is illustrated via a simple example. The time series having piece-wise constant slopes is shown in the top plot of Fig. 1.3. Shown in the second row are, respectively, the slice of its Gaussian smoothed surface at the first scale (left), the first-scale slice of its Gauss CWT (middle), and the first-scale slice of its Sombrero CWT (right). As can be observed from the time series, depicted in the top

plot of Fig. 1.3, there are slope changes at approximately 30 and 80 seconds, after which the time series becomes flat. The slice of the Gaussian smoothed surface (left bottom) is almost identical to the original signal (top) because Gaussian smoothing at low scales does not change the time series due to the very narrow span of the smoothing function. The slice of the Gauss CWT (middle bottom) is piece-wise constant with the magnitude of each segment being proportional to the time series slope. The slice of the Sombrero CWT contains two spikes at the points of slope change, representing the rate of change of slope of the time series.

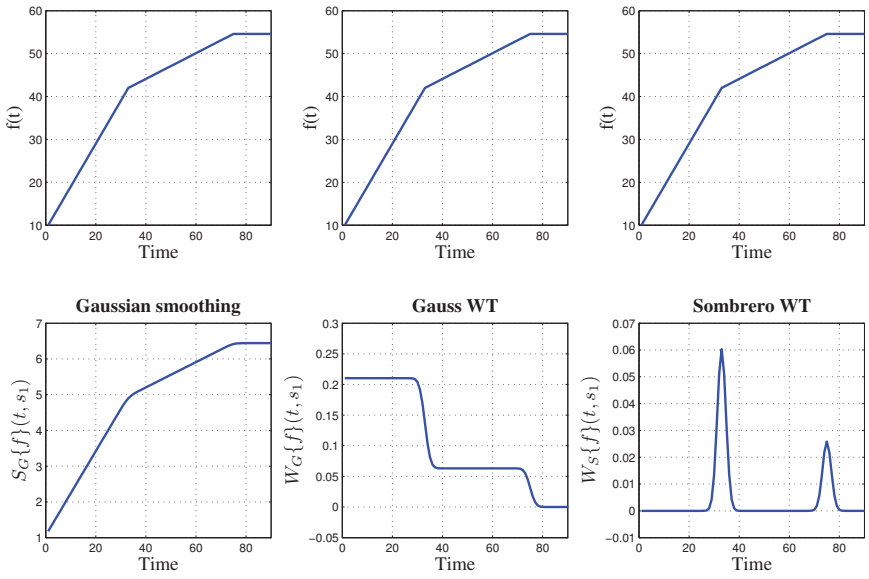

Figure 1.3. Example of features extracted from a time-series by different WTs

Another important feature of the CWTs relevant to PARSIM is their enhanced delineation of time series in the time-scale domain. To illustrate this point, let us consider the hypothetical output sensitivities ζ_1 and ζ_2 in the left plot of Fig. 1.4 associated with the hypothetical parameters θ_1 and θ_2. The two output sensitivities are nearly collinear with a correlation coefficient of $\rho = 0.9997$. Yet if the difference between their absolute normalized Gauss wavelet coefficients, $(|W\{\zeta_1\}|/\max|W\{\zeta_1\}|)-(|W\{\zeta_2\}|/\max|W\{\zeta_2\}|)$ were

considered, shown in the right plot of Fig. 1.4, one observes that it consists of both positive and negative values. This indicates that for each output sensitivity, there are regions of the time-scale plane wherein the absolute value of one output sensitivity's normalized wavelet coefficient exceeds the other's, albeit by a small margin. One can extrapolate these results to multiple output sensitivities, with the expectation that the regions associated with individual parameter signatures will become smaller with the overlap from the other output sensitivities' wavelet coefficients. However, given independent output sensitivities (i.e., full ranked Jacobian $\mathbf{\Phi}$) and adequate resolution in the time-scale plane (i.e., number of pixels), there will always be at least a pixel wherein the wavelet coefficient of each output sensitivity exceeds all the others.

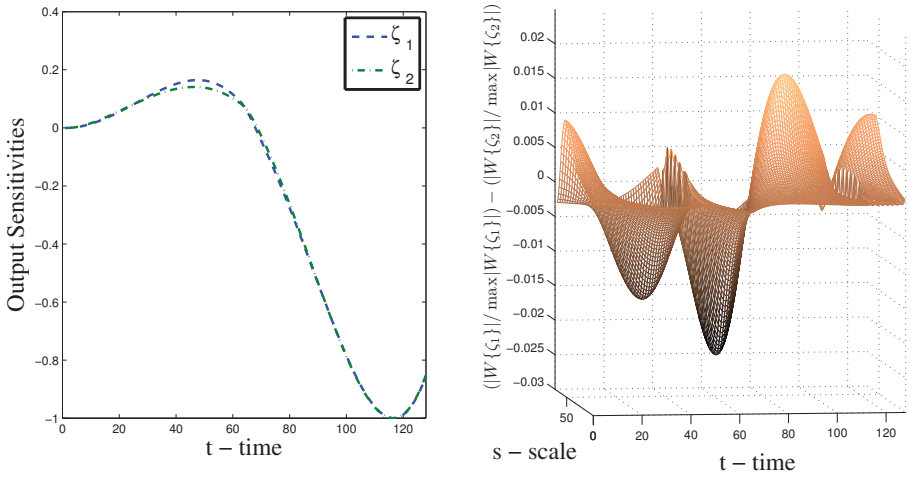

Figure 1.4. Two highly correlated output sensitivities and the difference between the absolute normalized values of their Gauss wavelet coefficients.

CHAPTER 2

THE ENGINE MODEL

The model used in this study is a generic engine model, provided by Pratt & Whitney, which is simulated by Numerical Propulsion System Simulation (NPSS^{TM}). The simulation is compiled and wrapped with an interface to allow it to be run using MATLAB/SIMULINK^{TM}. The schematic of the engine is shown in Fig. 2.1. The simulation is configured as a two-spool, high-bypass, separate flow turbofan and for the purpose of this study the health parameters are confined to the efficiency and flow capacity of the five major components: low pressure compressor (LPC), high pressure compressor (HPC), high pressure turbine (HPT), low pressure turbine (LPT), and fan. The ten health parameters used in this study are listed in Table 2.1. The flight conditions used for simulation are sea level static, standard day. The operation of the engine simulation is controlled by varying fuel flow. The simulated outputs that are measurable in-flight are also listed in Table 2.1.

The excitation input considered in this study to generate the transient outputs was a snap deceleration plus snap acceleration (V-shaped) input, which was emulated by running the simulation at high power for 15 seconds, ramping down the fuel flow for 10 seconds to approximately 80% power, and then ramping it back to full power for 10 seconds. Because the health parameters used in this study were functions of the power setting, this transient excursion was crafted so that the values of the parameters would not be overly influenced by the power setting. In every case in this study, the simulation was run to produce 40 seconds of outputs, and the excitation input was introduced at 14 seconds into simulation after the initial simulation transients had settled. As such, the transient outputs used for analysis were in the 14 - 38 second time-window.

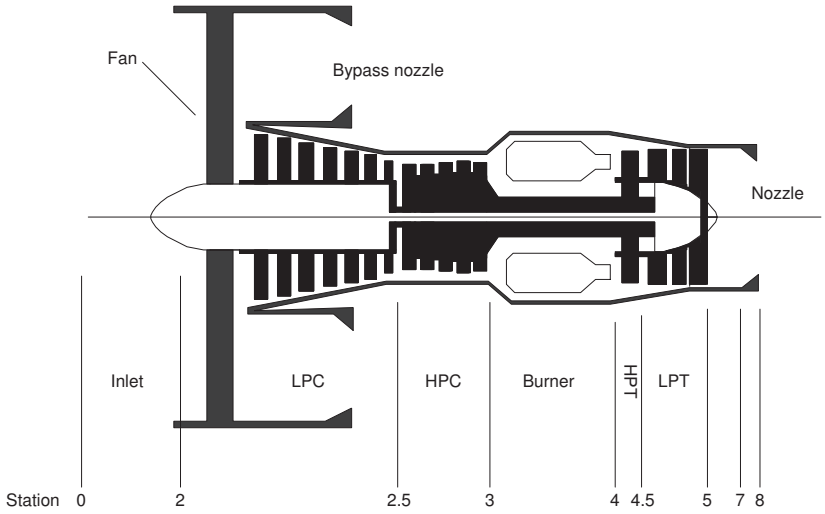

Figure 2.1. Schematic diagram of the two-spool, high-bypass, separate flow turbofan engine represented by the NPSS simulation model, together with the station and primary component locations

Table 2.1. The outputs simulated by the model, the engine components, and the health parameters. The numbering of the pressure and temperature outputs follows the standard aerospace practice for gas-turbine engines, see Fig. 2.1. The outputs simulated are those commonly measured in-flight. As to the parameters, the subscript "eff" denotes component efficiency, "FC" represents its flow capacity.

#	Output	#	Component	#	Parameter
1	Low Rotor Speed	1	Fan	1	$\Delta\text{Fan}_{\text{eff}}$
2	High Rotor Speed	2	LPC	2	$\Delta\text{Fan}_{\text{FC}}$
3	P2.5	3	HPC	3	$\Delta\text{LPC}_{\text{eff}}$
4	P3.0	4	HPT	4	$\Delta\text{LPC}_{\text{FC}}$
5	T3.0	5	LPT	5	$\Delta\text{HPC}_{\text{eff}}$
6	P5.0			6	$\Delta\text{HPC}_{\text{FC}}$
7	T5.0			7	$\Delta\text{HPT}_{\text{eff}}$
				8	$\Delta\text{HPT}_{\text{FC}}$
				9	$\Delta\text{LPT}_{\text{eff}}$
				10	$\Delta\text{LPT}_{\text{FC}}$

CHAPTER 3

THE DIRECT METHOD

DSIM is inspired by the heuristic approach of human experts who may attempt to identify the measured outputs affected by component degradation as a precursor to degraded component isolation. For this, also necessary is a knowledge of the outputs that ought to be affected by individual component degradations; i.e., degradation signatures. This is a typical pattern classification problem wherein the identification of affected measurements is achieved through signal processing and the isolation of the degraded component is obtained by mapping the affected measurements to the signatures of individual component degradations on the outputs. This dissertation will show, instead, that both the identification of the affected measurements and formulation of the component characteristic signatures are facilitated by the signal change detection introduced in this thesis.

The signal change detection presented in this thesis is achieved by isolating regions in the time-scale domain wherein the wavelet coefficients of individual outputs are considerably different from the others. The presence of such regions is used as indication of the effect of engine degradation on the output. This same approach is also applied to the sensitivities of modeled outputs to the health parameters to identify the outputs that are affected by individual health parameters. The latter is then used to establish the influence matrix representing the characteristic signatures of the health parameters for isolating the degraded components.

The basis for defining in DSIM the characteristic signatures of the components on the outputs is the sensitivity of the transient engine outputs to health parameters. The underlying analogy is that if degradation of individual components is reflected in the corresponding

health parameters, as is assumed in the inverse approach, then the sensitivity of the outputs to individual health parameters should provide a blueprint for the characteristic signatures of components. The shape representation capacity of continuous wavelet transforms is used to account for various shape attributes of the transient outputs/residuals, and the enhanced delineation of these outputs/residuals for change detection [34].

3.1 Residual Flagging

A residual, $\epsilon_j(t)$, is defined here as the difference between the measured output, $y_j(t)$, and its baseline trace, $y_j^n(t)$, in response to a known and pre-specified excitation input, $\mathbf{u}(t)$, as

$$\epsilon_j(t|\mathbf{u}(t)) = y_j(t|\mathbf{u}(t)) - y_j^n(t|\mathbf{u}(t)) \qquad t \in [t_1, t_N] \tag{3.1}$$

As such, it is assumed here that measurements are obtained by introducing a pre-specified excitation to the engine every so often; e.g., once during each cycle or that they are obtained during take-off. The residuals would then represent the difference between these measurements and their normal trace already archived for the engine previously. A sample of such simulated residuals, during the transients caused by the V-shaped fuel flow to the engine, is shown in Fig. 3.1. As is clear from the results, the size of the residuals are too small to be used for their delineation in the time domain. However, there is considerable difference between the shapes of these residuals which can be used as the basis to characterize their differences. The shape representation capacity of the CWTs [27] is of particular use in this endeavor.

Another feature of the CWTs that is essential to the identification of degradation-affected residuals is the enhanced delineation CWTs provide in the time-scale domain [26]. For distinction of local differences between the residuals, the notion of *degradation signature* is introduced as:

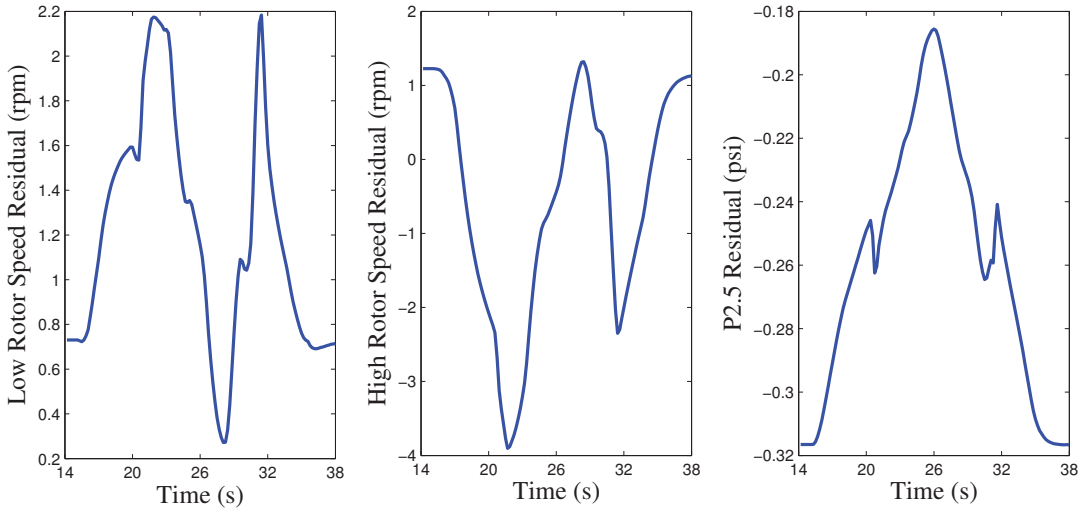

Figure 3.1. The residuals of the first three outputs representing degradation in LPC

Definition 1 If a pixel (t_k, s_l) exists which satisfies the following condition

$$\left|\overline{W\{\epsilon_j\}}(t_k, s_l)\right| > \eta_d \left|\overline{W\{\epsilon_m\}}(t_k, s_l)\right| \quad \forall\, m = 1, \ldots, p \neq j \tag{3.2}$$

where p denotes the number of outputs in the output suite, η_d is the *dominance factor*, and

$$\overline{W\{\epsilon_j\}} = \frac{W\{\epsilon_j\}}{\max_{(t,s)} |W\{\epsilon_j\}|} \tag{3.3}$$

then the pixel is labeled as (t_k^j, s_l^j) and included in $\mathcal{R}_j$, the *degradation signature* associated with ϵ_j.

The normalization of the wavelet coefficients according to Eq. (3.3) nullifies the dependence of the wavelet coefficients on the amplitude of $\epsilon_j(t)$ in Eq. (3.2) and leaves the correlation between the residual $\epsilon_j(t)$ and the wavelet $\psi_s(t)$ in Eq. (1.2) as the only factor affecting the magnitude of the CWT at each time and scale. Accordingly, a signal $\epsilon_1(t)$ that is only slightly different from $\epsilon_2(t)$ in a time-window, associated with the dilation width of

the wavelet at a certain scale, will correlate differently than $\epsilon_2(t)$ with $\psi_s(t)$ within that time-window, hence, accentuating their local differences.

For illustration purposes, the degradation signatures of the three residuals in Fig. 3.1 obtained at $\eta_d = 1.75$ via the Gauss CWT are shown in Fig. 3.2, where the dark pixels in the plane represent the locations where the wavelet coefficient of the corresponding residual is dominant relative to that of the rest of the residuals in the output suite. Since, as discussed earlier, the Sombrero CWT represents the rate of slope changes of the time series in the time-scale domain, the degradation signatures shown in Fig. 3.2 represent the regions where the slope of the corresponding residual is larger than all the others in the suite of seven residuals available on-board.

The presence of a degradation signature in DSIM is used as indication of the unique effect of degradation on the output, hence, the identifiability of degradation through the output. This identifiability is represented by assigning binary values to those residuals which have more than a designated number of pixels in the degradation signature, as

$$|\epsilon_j| = \begin{cases} 1 & \sum_{k=1,l=1}^{N,M}(t_k^j, s_l^j \in \mathcal{R}_j) > d \\ 0 & \text{otherwise} \end{cases} \tag{3.4}$$

where $|\epsilon_j|$ is the binary flag value associated with ϵ_j and $d \in \mathbb{N}$ is called the *signature size threshold* representing the designated number of pixels. The above flagging approach implements a binary strategy in accordance with the notion of degradation signatures indicating the effect of degradation on the output. An alternative approach here would be a non-binary strategy whereby the flag value is assigned according to the quality of the signature, but as yet no solid criterion for such a quality measure has been conceived and the analysis is currently restricted to the binary approach.

As is clear from Eq. (3.2), the value of the dominance factor, η_d, is central to the estimation of degradation signatures. Higher dominance factors lead to fewer pixels in the

degradation signatures at the risk of missing minute differences between the residuals. Accordingly, higher dominance factors would correspond to higher standards of identifiability for degradation. Also central to estimation of degradation signatures is the wavelet transform used, as the flagged residuals would be different for different wavelet transforms. Here no additional subscript to signify the type of wavelet transform used, but alert the reader that the flag value will be different given the wavelet transform, the dominance factor and the signature size threshold used.

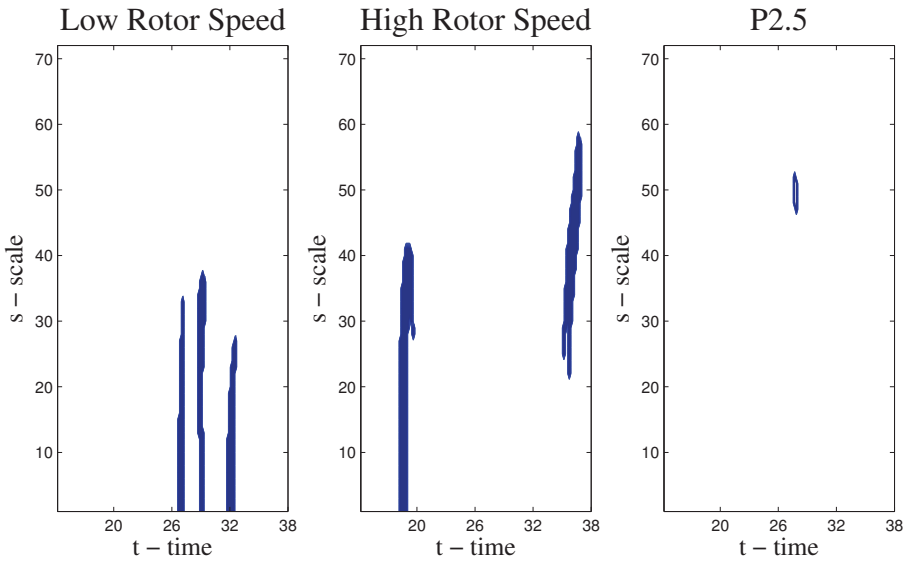

Figure 3.2. The degradation signatures of LPC by the Gauss WT at $\eta_d = 1.75$ extracted from the residuals in Fig. 3.1

For illustration purposes, the flagged residuals for a new engine by the Gauss CWT at $\eta_d = 1.75$, $\eta_d = 2$, and $\eta_d = 2.25$ using the signature size threshold of $d = 5$ obtained according to Eq. (3.1) are shown in Table 3.1. For this case, $y_j^n(t|\mathbf{u}(t))$ in Eq. (3.1) was simulated to correspond to a new engine and the degraded components were simulated to represent degradation levels associated with approximately 1000 cycles. The degradation signatures were obtained according to Eq. (3.2) using the Gauss WT and flagged according to Eq. (3.4) at the signature size threshold of $d = 5$. As is clear from the results, some

of the flag values change from 1 to 0 at higher dominance factors, indicating diminished identifiability of degradation by the residuals at higher dominance factors. Corresponding to the residual signatures in Fig. 3.2 are the first three flagged residuals in Table 3.1 for LPC at $\eta_d = 1.75$, which indicate that each of the residual signatures in fig. 3.2 have more pixels than $d = 5$.

Table 3.1. The flagged residuals according to Eq. (3.4) by the Gauss WT at the three different dominance factors of $\eta_d = 1.75$, $\eta_d = 2$ and $\eta_d = 2.25$ with $d = 5$

Output #	**Degraded Component**														
	Fan			**LPC**			**HPC**			**HPT**			**LPT**		
	η_d			η_d			η_d			η_d			η_d		
	1.75	2.0	2.25	1.75	2.0	2.25	1.75	2.0	2.25	1.75	2.0	2.25	1.75	2.0	2.25
1	0	0	0	1	1	1	0	0	0	0	0	0	1	0	0
2	1	1	1	1	1	1	1	1	1	1	1	0	1	1	1
3	0	0	0	1	0	0	1	1	1	1	1	0	1	0	0
4	1	1	1	0	0	0	1	1	1	0	0	0	0	0	0
5	0	0	0	0	0	0	1	0	0	1	1	1	1	1	1
6	1	1	1	1	1	1	1	0	0	1	1	1	1	1	1
7	0	0	0	1	1	1	1	1	1	1	1	1	1	1	1

3.2 Influence Matrices

Once the flagged residuals have been obtained, they need to be attributed to a component degradation. In DSIM, the relationship between the flagged residuals and degraded components is established according to the sensitivity of the model outputs to either components or health parameters. Furthermore, in order to comply with the practical constraint of unknowable health parameters for the engine, the influence matrices are estimated only once in this study by setting the value of each health parameter to 1 to represent the engine at 0-cycle.

3.2.1 According to Component Sensitivity

One approach to establishing the 'a priori' relationship between the outputs and component degradations is to assume that any degradation of a component is associated with changes to its efficiency and flow capacity parameters. Accordingly, the sensitivity of the outputs to the individual components can be estimated as

$$\partial \hat{y}_j / \partial C_i = \frac{\hat{\mathbf{y}}(\mathbf{u}(t), \bar{\mathbf{\Theta}} - \delta\theta_{2i} - \delta\theta_{2i+1}) - \hat{\mathbf{y}}(t, \mathbf{u}(t), \bar{\mathbf{\Theta}})}{\delta\theta_{2i} + \delta\theta_{2i+1}} \tag{3.5}$$

where $\bar{\mathbf{\Theta}}$ denotes the vector of nominal parameter values for the engine (all set to 1 for a 0-cycle engine), and $\delta\theta_{2i}$ and $\delta\theta_{2i+1}$ represent perturbations of the efficiency and flow capacity of the component C_i. It should be noted here that the negative perturbations in Eq. (3.5) are not necessarily representative of all the health parameter changes by degradation, since the flow capacity values increase with turbine degradations. As a potential alternative, one could use a central difference approach to include both positive and negative perturbations, at the cost of performing twice as many simulation runs. Using the component sensitivity of the outputs, one can adopt the same strategy as in degradation signatures to define the *output/component signature* as:

Definition 2 If a pixel (t_k, s_l) exists which satisfies the following condition

$$\left|\overline{W\{\partial \hat{y}_j / \partial C_i\}}(t_k, s_l)\right| > \eta_d \left|\overline{W\{\partial \hat{y}_q / \partial C_i\}}(t_k, s_l)\right| \quad \forall\, q = 1, \ldots, p \neq j \tag{3.6}$$

where p denotes the number of outputs in the output suite and $\overline{W\{\partial \hat{y}_j / \partial C_i\}}$ is normalized as in Eq. (3.3), then the pixel is labeled as (t_k^j, s_l^j) and included in Ω_{ji}, the *output/component signature* of C_i on the output y_j.

The presence of a output/component signature, as defined above, indicates that the corresponding output in the output suite is affected by the combined parameter perturbations of the component. As such, the output/component signatures are used to provide

a blueprint of the component effects on the outputs. But before the utility of the output/component signatures in the analysis is discussed, it is worthwhile mentioning their similarities/differences with the degradation signatures. The output/component signatures are similar to the degradation signatures in that they too consider the dominance of individual outputs in an output suite. They differ from the degradation signatures, however, in that the output/component signatures are model-based, because of their reliance on the modeled output; i.e., $\partial\hat{y}_j/\partial C_i$, whereas the residuals are empirical and obtained from the actual engine.

The output/component signatures, similar to the degradation signatures, provide the basis for identifying the outputs that are dominantly effected by individual components. As before, the presence of a output/component signature is used as indication of the component influence on the corresponding output, and implement the following binary flagging approach to the component sensitivities

$$|\partial\hat{y}_j/\partial C_i| = \begin{cases} 1 & \sum_{k=1,l=1}^{N,M}(t_k^j, s_l^j \in \Omega_{ji}) > d \\ 0 & \text{otherwise} \end{cases} \tag{3.7}$$

where d is the signature size threshold, as in Eq. (3.4). Using the above flagging scheme, each flagged component sensitivity represents a component of an influence matrix to be used to estimate component degradation values according to the flagged residuals vector.

For illustration purposes, shown in Table 3.2 is the influence matrix comprising the flagged component sensitivity values according to the perturbation size of $\delta\theta_i = 0.002$ in Eq. (3.5), using the Gauss WT, the dominance factor of $\eta_d = 1.75$, and signature size threshold of $d = 5$. The perturbation size of $\delta\theta_i = 0.002$ will be uniformly the same for all the parameters in all cases of sensitivity computation in this paper, and is selected to be small enough to comply with the notion of using the difference equation as approximation to differentiation.

Table 3.2. The binary influence matrix comprising the flagged component sensitivity values of the outputs by the Gauss WT at the dominance factor of $\eta_d = 1.75$ and signature size threshold of $d = 5$. The 1's in this table represent the influence of the component on the corresponding output.

Output #	Component				
	Fan	**LPC**	**HPC**	**HPT**	**LPT**
1	0	1	0	0	1
2	1	1	1	1	1
3	0	1	1	1	1
4	1	0	1	1	0
5	0	0	1	1	1
6	1	1	0	0	1
7	0	1	1	1	1

According to the influence matrix in Table 3.2, the outputs that may be potentially affected by each component degradation have a magnitude of 1 in the row associated with the component. For example, according to the results in this table a degradation in LPC is expected to influence outputs 1, 2, 3, 6, and 7. But the more interesting result in this table is that both HPC and HPT affect the same outputs, therefore, they are indistinguishable with this influence matrix. To bypass cases such as this, where the components blueprint influence on the outputs is the same, several influence matrices will be estimated according to both the Gauss and Sombrero CWTs and three different dominance factors.

3.2.2 According to Parameter Sensitivity

The second approach to establishing the 'a priori' relationship between the outputs and engine components is through the health parameters. According to this scheme, the flagged residuals are first associated with individual health parameters and then with engine components. The parameter sensitivities are generated as

$$\partial \hat{y}_j / \partial \theta_i \approx \frac{y_j(\mathbf{u}(t), \bar{\mathbf{\Theta}} + \delta\theta_i) - y_j(\mathbf{u}(t), \bar{\mathbf{\Theta}})}{\delta\theta_i} \tag{3.8}$$

where $\bar{\mathbf{\Theta}}$ is the vector of nominal parameter values, all set to 1 in this study, θ_i is an individual health parameters, among those listed in Table 2.1, and $\delta\theta_i$ represents the perturbation size of the parameter (0.002 in this study). Here, instead of positive perturbations, one could use negative perturbations, as in Eq. (3.5), or both positive and negative perturbations for a central difference approach. Assessing the suitability of the approximation scheme is deferred to when the method is studied for practical implementation. As before, one can define the *output/parameter signature* as

Definition 3 If a pixel (t_k, s_l) exists which satisfies the following condition

$$\left|\overline{W\{\partial\hat{y}_j/\partial\theta_i\}}(t_k, s_l)\right| > \eta_d \left|\overline{W\{\partial\hat{y}_q/\partial\theta_i\}}(t_k, s_l)\right| \quad \forall\ q = 1, \ldots, p \neq j \tag{3.9}$$

where p denotes the number of outputs in the output suite and $\overline{W\{\partial\hat{y}_j/\partial\theta_i\}}$ is normalized as in Eq. (3.3), then the pixel is labeled as (t_k^j, s_l^j) and included in Π_{ji}, the *output/parameter signature* of θ_i on the output y_j.

As with the previous signatures, a higher dominance factor provides a higher level of resolution at the risk of ignoring minor differences. Similar to the component sensitivities, the parameter sensitivities in DSIM are flagged as

$$|\partial\hat{y}_j/\partial\theta_i| = \begin{cases} 1 & \sum_{k=1,l=1}^{N,M}(t_k^i, s_l^i \in \Pi_{ji}) > d \\ 0 & \text{otherwise} \end{cases} \tag{3.10}$$

where d is the signature size threshold used in Eq. (3.4). Using the flagged parameter sensitivities, a similar influence matrix as the one in Table 3.2 can be formed. For illustration purposes, the influence matrix according to parameter sensitivities obtained at the dominance factor of $\eta_d = 1.75$ via Gauss CWT and based on the signature size threshold of $d = 5$ is shown in Table 3.3. According to the influence matrix in this table, parameters

7 and 8: $\Delta\text{HPT}_{\text{eff}}$ and $\Delta\text{HPT}_{\text{FC}}$, affect the same outputs: 2, 3, 5 and 7, but there is no other redundancy observed with the other parameters.

Table 3.3. The binary influence matrix obtained by parameter sensitivity of the outputs at the dominance factor of $\eta_d = 1.75$ via Gauss WT with $d = 5$ to represent the influence of each parameter on the outputs

Output #	**Parameter #**									
	1	**2**	**3**	**4**	**5**	**6**	**7**	**8**	**9**	**10**
1	1	0	1	1	0	0	0	0	0	1
2	1	1	0	1	1	1	1	1	0	0
3	1	0	1	0	1	1	1	1	1	1
4	1	1	0	1	0	0	0	0	1	0
5	0	0	0	0	0	1	1	1	1	1
6	1	1	1	1	0	1	0	0	1	0
7	0	0	0	1	1	1	1	1	0	1

3.3 Degradation Estimation

Let us consider the case where the presence of engine degradation is suspected. As a side note, although degradation detection is not addressed in this thesis, it is not consider as challenging as degradation isolation since it has been observed that degradation detection to be possible through a variety of mechanisms such as cumulative sum of residuals or Gaussian smoothed-based degradation signatures. The formulation of such mechanism is deferred until the practical implementation of the DSIM is considered, so as to base its design on real data from the engine.

In each degradation scenario, the flagged residuals, on the one hand, specify the outputs that are affected by the degraded component. The influence matrices, on the other hand, provide an account of the outputs that are expected to be affected by each component or parameter. As such, each flagged residual when mapped through the influence matrix can provide an account of the components or health parameters that are likely to have been responsible for the flagged residuals.

3.3.1 Based on Component Sensitivity

Consider the flagged residual vector, $\mathbb{E}$, below obtained by the Gauss WT at the dominance factor of $\eta_d = 1.75$ and signature size threshold of $d = 5$ as the result of degradation of HPT, as

$$\mathbb{E} = [|\epsilon_j|] = \begin{bmatrix} 1 & 1 & 0 & 1 & 1 & 0 & 1 \end{bmatrix}^T$$

The components of the residual vector above are sequenced according to the output number in Table 2.1. Mapping this flagged residual vector against the influence matrix in Table 3.2, which is obtained with the same CWT, dominance factor and signature size threshold, can be readily achieved by the cosine similarity of the above residual vector to the individual columns of the influence matrix in Table 3.2. According to this strategy, the individual *component degradation estimates* $\widehat{\Delta C}_{mc}$ according to component sensitivities (denoted by the subscript c) are obtained as

$$\widehat{\Delta C}_{mc} = \frac{\sum_{j=1}^{p} |\epsilon_j| \times |\partial \hat{y}_j / \partial C_m|}{\sqrt{\sum_{j=1}^{p} \left(|\epsilon_j|\right)^2} \sqrt{\sum_{j=1}^{p} \left(|\partial \hat{y}_j / \partial C_m|\right)^2}} \tag{3.11}$$

which for the example flagged residual above produces the following normalized component estimate

$$\widehat{\mathbf{\Delta C}}_c = \begin{bmatrix} 0.56 & 0.6 & 0.8 & 0.8 & 0.73 \end{bmatrix}^T$$

which provides the highest estimates for the HPT as well as the HPC. As will be shown later, the overall estimate for each component will consist of those from Gauss and Sombrero CWTs at several dominance factors to provide a better resolution for component degradation estimates than the single estimate shown above.

3.3.2 Based on Parameter Sensitivity

Obtaining the component degradation estimates according to parameter sensitivities is a bit more involved, since the parameter sensitivities can only be useful for narrowing

down the list of health parameters potentially affected by the engine degradation. Given that several residuals are usually flagged in each degradation scenario and each residual (output) is associated with a different set of health parameters, a voting scheme is devised here to integrate the count for health parameters from different flagged residuals. In this voting scheme, the *parameter count*, $\Sigma\theta_i$, is computed to represent the number of times a health parameter is counted by all the flagged residuals as

$$\Sigma\theta_i = \sum_{j=1}^{p} |\epsilon_j| \times |\partial\hat{y}_j/\partial\theta_i| \tag{3.12}$$

The goal of the parameter count, however, is to identify the degraded component, which can be traced to either or both its efficiency and flow capacity. To this end, the *component count*, ΣC_m, is computed as the sum of the corresponding health parameters, as

$$\Sigma C_m = \Sigma\theta_i + \Sigma\theta_{i+1}, \quad i = 2m-1 \ \text{ for } \ m = 1, \ldots, Q/2 \tag{3.13}$$

where Q is the number of health parameters and $Q/2$ denotes the number of components in the engine. For illustration purposes, let us consider again the flagged residual vector $\mathbb{E}$ above, which according to Eq. (3.12) and the influence matrix in Table 3.3 yields the parameter count vector

$$\mathbf{\Sigma}\theta = \begin{bmatrix} 3 & 2 & 1 & 4 & 2 & 3 & 3 & 3 & 2 & 3 \end{bmatrix}^T,$$

sequenced according to the parameter numbers in Table 2.1. Using Eq. (3.13), the above parameter count results in the component count vector

$$\mathbf{\Sigma C} = \begin{bmatrix} 5 & 5 & 5 & 6 & 5 \end{bmatrix}^T$$

which provides the component count of 8 for the HPT. But the above component count does not yet provide a definitive estimate of the component degradation, due to the uneven

representation of the parameters/components in the influence matrix. That is, if one were to consider the scenario where all the residuals were flagged, then the resulting component count vector would represent the total count of each component in the influence matrix, hereafter referred to as the *component weight*, ΣW. For example, the component weight for the influence matrix in Table 3.3 is

$$\mathbf{\Sigma}W = \begin{bmatrix} 8 & 8 & 8 & 8 & 8 \end{bmatrix}^T$$

which has equal weight for all the components. Using the component weights to calibrate the component count, the component degradation estimate, $\widehat{\Delta C}_{m\theta}$, according to parameter sensitivities (denoted by the subscript θ) is computed as

$$\widehat{\Delta C}_{m\theta} = \frac{\Sigma C_m / \Sigma w_m}{\sum_{m=1}^{Q/2} \widehat{\Delta C}_{m\theta}} \tag{3.14}$$

which represents the ratio of the component count to component weight of each component, normalized across all the component degradation estimates. Using the above formula, the normalized component degradation estimate for our example is computed as

$$\widehat{\mathbf{\Delta C}}_\theta = \begin{bmatrix} 0.192 & 0.192 & 0.192 & 0.23 & 0.192 \end{bmatrix}^T$$

which provides the highest estimates for the HPT.

3.4 Degradation Isolation Results

Practical application of DSIM entails obtaining the residuals by subtracting from the current sensory data the baseline data collected from the engine before, transforming the residuals to the time-scale domain by Gaussian smoothing and/or the Gauss and Sombrero

CWTs, extracting the residual signatures and flagging them, and then mapping the flagged residuals through the influence matrix that is available 'a priori' from the engine.

In practice, DSIM will use as baseline the sensory data obtained from the engine prior to its current application. This baseline data can be collected as frequently as possible so that the flagged residuals can comprise potential gradual degradation of various components. However the influence matrix cannot be computed as frequently, since it would require knowledge of the health parameters. The influence matrix in this study is computed for the new engine (with the health parameters set to 1) under the flight conditions the transient data will be collected and used throughout for engines of different ages. In the absence of actual sensory data, the baseline data are obtained from simulation.

Apart from practical concerns such as measurement noise, there are two concerns associated with DSIM's performance. One is the validity of using an influence matrix that may not necessarily represent the current engine condition and age. The other is the repeatability of degradation isolation for different levels of component degradation. As such, a test was designed to evaluate DSIM's repeatability at different engine ages. DSIM's performance is then demonstrated in a case closer to its envisioned application, which is periodic monitoring of component degradations. This "illustrative case" is also used to demonstrate the potential effect of some of the practical issues faced in practice, such as measurement noise, sensor bias and different flight conditions. In all cases, the transient outputs of the V-shaped input, described in Chapter 2, were used for data generation.

3.4.1 Repeatability Test

Degradation cases were simulated for three engine ages: new (0 cycle), 1000 cycles and 2000 cycles. The NPSS model has the capability to simulate the performance of gas-turbines in service, i.e., engine components degraded to higher cycle counts. This is accomplished via scalars to the efficiency and flow capacity of the respective component maps. For instance, to test DSIM for a new engine with degradation in the LPC, all scalars

were set to their default values, except for those of the LPC, which were set to a level equal to approximately 1000 cycles of degradation. To test the statistical robustness of DSIM, ten separate random component degradation episodes for each component corresponding to roughly 1000 ± 50 cycles from the nominal degradation for each component were processed. Component degradation episodes were also simulated for engines in service, at 1000 and 2000 cycles. Similarly, for engines in service, the scalars were set to values corresponding to higher cycle counts to reflect the deterioration of all components, while the scalars of the component under test were set at elevated levels (i.e., the degraded component of the 2000-cycle engine was set at the degradation of 3000 ± 50 cycles). Ten separate random episodes of each component degradation were considered for each engine age as well. It is a well established fact that an engine fleet average deterioration trend does not exist and that each engine will follow its own unique degradation profile. Given that DSIM's operation does not depend on the existence of such profile, only the averages were used to establish a baseline for the health parameter values at the corresponding engine age. Alternatively, randomly deviated health parameters from some nominal set of parameter values to depict engine degradation could have been employed, but such a scheme would not have been reflective of the number of cycles the depicted degradations were associated with.

A sample of health parameter deviations from their norm used in the simulation runs is listed in Table 3.4. From the small magnitude of the health parameter deviations in Table 3.4, it is clear that DSIM was challenged to isolate small component degradations, but this was done to test the lower range of DSIM's isolation ability as assurance of its success for larger degradation levels. Larger degradations are generally associated with more pronounced residual differences that not only improve the accuracy of diagnostics but also reduce the impact of measurement noise on isolation.

Table 3.4. Sample of parameter deviations used in the simulation to represent degradation of individual components of the engine

Associated Health Parameters Deviations									
Fan		**LPC**		**HPC**		**HPT**		**LPT**	
-0.0030	-0.0016	-0.0058	-0.0078	-0.0042	-0.0024	-0.00099	0.00072	-0.0014	0.0016

For each case of the test, the residuals were obtained according to Eq. (3.1) with $y_j^n(t|\mathbf{u}(t))$ obtained at the health parameters representing the age of the engine (i.e., equal to 1 for a new engine or levels corresponding to engines with 1000 or 2000 cycles of service). The degradation signatures were then obtained according to Eq. (3.2) with Gauss and Sombrero CWTs for each of the 150 simulated output sets (i.e., 10 episodes $\times$ 5 components $\times$ 3 engines). These residuals were then flagged according to Eq. (3.4) at the signature size threshold of $d = 5$ and used to estimate the component degradation estimates according to both component and parameter sensitivities, Eqs. (3.11) and (3.14), respectively. For illustration purposes, samples of the component degradation estimates representing correct diagnosis, split diagnosis, and misdiagnosis are shown in Table 3.5. According to the terminology demonstrated in this table, "correct diagnosis" is represented by a diagnostic accuracy (DA) of 1 to indicate a match between the highest component degradation estimate, $\widehat{\Delta C_m}$, and the simulated component degradation. In "split diagnosis," the DA is set as the inverse of the number of equal high component degradation estimates, so long as one of them coincides with the simulated component degradation (DA = 1/2 in the table). "Misdiagnosis" (DA = 0) denotes the mismatch between the highest $\widehat{\Delta C_m}$ and the simulated component degradation.

As mentioned earlier, the component degradation estimates can be obtained from either the Gauss or Sombrero CWT. As such, these estimates need to be integrated to provide a comprehensive account of the different aspects of the output shapes, represented by the CWT, and the level of dominance denoted by the dominance factor, η_d. It was chosen to perform this integration by adding all the estimates, as depicted in Table 3.6 for a case when

Table 3.5. Illustration of the three categories of diagnostic accuracy applied to the normalized component degradation estimates

Degraded Component	**Correct Diagnosis** $DA = 1$		**Split Diagnosis** $DA = 1/2$		**Misdiagnosis** $DA = 0$	
	$\mathbf{\Delta C}$ Real	$\widehat{\mathbf{\Delta C}}$ Estimate	$\mathbf{\Delta C}$ Real	$\widehat{\mathbf{\Delta C}}$ Estimate	$\mathbf{\Delta C}$ Real	$\widehat{\mathbf{\Delta C}}$ Estimate
Fan	0	0.2083	0	0.1917	0	0.1921
LPC	**1**	**0.2239**	0	0.1831	0	0.1806
HPC	0	0.2167	0	**0.2240**	**1**	0.2140
HPT	0	0.1862	**1**	**0.2240**	0	**0.2194**
LPT	0	0.1650	0	0.1773	0	0.1940

the Fan was degraded. The last column of Table 3.6 is the normalized sum of the other six columns. According to the results in this table, the highest estimates by the Gauss CWT at the dominance factor of $\eta_d = 1.75$ (first column) are split between the Fan and the LPC, the highest estimate at the dominance factor of $\eta_d = 2$ (second column) is correct, but it is erroneous at $\eta_d = 2.25$ (third column). The estimates by the Sombrero CWT (columns 4-6), on the other hand, are all correct in isolating the simulated degradation. By summing the estimates from the two wavelet transforms, the majority estimate is captured, which happens to be correct in this case. It was observed that the inclusion of all the estimates in the integrated results provides the most robust and unbiased set of estimation results for the cases considered.

Using the accuracy count in Table 3.5, the diagnostic accuracy for all the simulated component degradations according to component and parameter sensitivities are shown in Table 3.7. Each component degradation estimate in this table represents the sum of six degradation estimates, as illustrated in Table 3.6, obtained from the Gauss and Sombrero CWTs at the dominance factors of $\eta_d = 1.75$, $\eta_d = 2.0$ or $\eta_d = 2.25$, and flagged with the signature size threshold of $d = 5$. The diagnostic accuracy values in this table represent the fraction of accurate isolations of the 10 episodes simulated for each component degradation.

Table 3.6. Illustration of integration by summation of component degradation estimates by Gauss and Sombrero CWTs at different dominance factors, yielding the normalized composite degradation estimates for each degradation case

	$\widehat{\mathbf{\Delta C}}$							
	Gauss WT			**Sombrero WT**				$\overline{\sum \widehat{\mathbf{\Delta C}}}$
	$\eta_d = 1.75$	$\eta_d = 2$	$\eta_d = 2.25$	$\eta_d = 1.75$	$\eta_d = 2$	$\eta_d = 2.25$		
	0.2258	0.2614	0.2264	0.2136	0.2120	0.2095		0.2239
	0.2258	0.2490	0.2358	0.1988	0.1983	0.1956		0.2167
$\sum$	0.1935	0.1992	0.1415	0.1958	0.1939	0.1956	$\Longrightarrow$	0.1862
	0.1613	0.1162	0.1132	0.1958	0.2019	0.1956		0.1650
	0.1935	0.1743	0.2830	0.1958	0.1939	0.2037		0.2083

According to the results obtained by component sensitivity for the new engine in this table, degradations of all components except the LPT are isolated in every case, and that the estimates by parameter and component sensitivities are not the same.

Table 3.7. The diagnostic accuracy values using the component and parameter sensitivities of the new engine. The estimates are the normalized sum of individual estimates by Gauss and Sombrero CWTs at the three dominance factors of $\eta_d = 1.75$, $\eta_d = 2.0$ and $\eta_d = 2.25$ using the signature size threshold of $d = 5$.

Engine Age	**Overall Accuracy**	**Diagnostic Accuracy (DA)** Fan	LPC	HPC	HPT	LPT
		based on component sensitivity				
new (0-cycle)	84%	10/10	10/10	10/10	10/10	2/10
1000-cycle	80%	10/10	10/10	10/10	10/10	0/10
2000-cycle	74%	10/10	10/10	5/10	8/10	4/10
		based on parameter sensitivity				
new (0-cycle)	74%	10/10	7/10	10/10	10/10	0/10
1000-cycle	82%	10/10	3/10	10/10	10/10	8/10
2000-cycle	62%	10/10	3/10	1/10	10/10	7/10

An aspect of the component degradation estimates that is not represented by the results in Table 3.7 is the inherent bias in the estimates that can be exploited to advantage. An example of this bias corresponds to the component degradation estimates by parameter

sensitivity for LPT, which all point to the HPT, or that every misdiagnosis of the LPC is in favor of the HPC. For illustration purposes, shown in Fig. 3.3 is the bias of the component degradation estimates toward HPT when LPT is degraded (shown by the dashed vertical line in the figure). According to this bias, whenever HPT is diagnosed as the degraded component according to parameter sensitivity, there is equal likelihood that it could be the surrogate for LPT. Here, the degradation estimates can be used by the component sensitivity to advantage, since the results are complementary in nature. Consider, for instance, the estimates for the new engine in Table 3.7 by parameter sensitivity: they all misdiagnose LPT whereas they are 20% accurate by component sensitivity, or the estimates for LPC which are only at 70%, whereas they are perfect by component sensitivity. Using the observed bias such as those mentioned above, one can define rules to further improve the accuracy of isolation by the two sensitivities. A set of such rules have been implemented, as shown in Table 3.8, to illustrate the potential improvements possible.

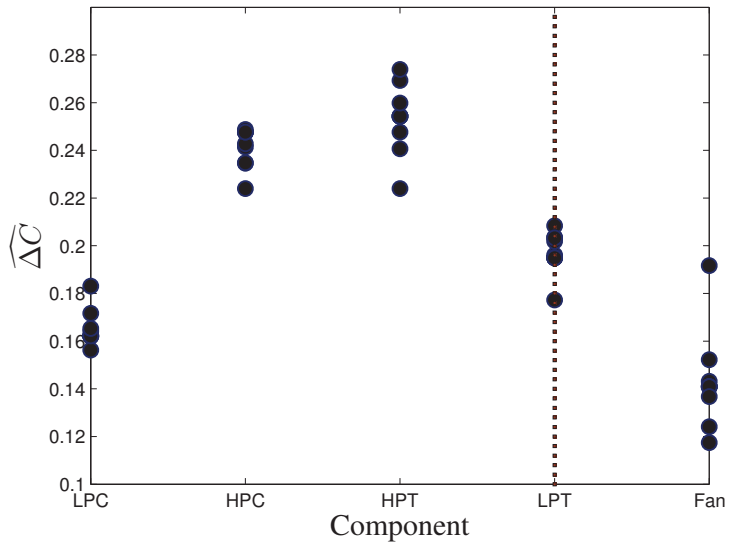

Figure 3.3. Sample of bias among the component degradation estimates - HPT is consistently selected when the target component degradation is LPT (indicated by the vertical line)

According to the first rule shown in Table 3.8, whenever LPC is selected according to either the parameter sensitivity (par_sen) or component sensitivity (comp_sen) then LPC should be selected as the degraded component. This rule is supported by the observation that both parameter and output sensitivities are consistent in diagnosing degradation in LPC. The second rule, on the other hand, accounts for the misdiagnosis of LPC degradation by parameter sensitivity for HPC and uses the estimate by component sensitivity in favor of LPC estimation. The last rule uses the estimate of LPT by component sensitivity to overrule the estimate of HPT by parameter sensitivity. The set of rules devised in Table 3.8 are not optimal and are only shown to indicate the potential for improving the results by integrating the two estimates from parameter and component sensitivities.

Table 3.8. The set of rules to consolidate the component degradation assessments from component and parameter sensitivities

If par_sen $\longrightarrow$ LPC	or	comp_sen $\longrightarrow$ LPC	then	deg_comp = LPC
If par_sen $\longrightarrow$ HPC	and	comp_sen $\longrightarrow$ LPC	then	deg_comp = LPC
If par_sen $\longrightarrow$ HPT	and	comp_sen $\longrightarrow$ LPT	then	deg_comp = LPT

Using the rules shown in Table 3.8, the estimates in Table 3.7 were refined as shown in Table 3.9. The results indicate that the component degradation estimates are clearly improved over those obtained by parameter estimates. It is, however, puzzling that the results for the 2000-cycle engine are relatively weak, particularly that the results for the 1000-cycle engine are improved relative to those for the new engine. A possible explanation for the weaker results of the 2000-cycle engine is that if one were to plot the component deterioration with respect to cycle count, one would immediately notice that there is a significant slope change (slope becomes much more shallow) between 1000 and 2000 cycles. This reduction in the level of deterioration may be causing the degradation effects less prominent thereby eroding the effectiveness of the DSIM for the 2000-cycle engine. Another explanation could be the deviation of this older engine behavior from that of the new

engine, hence the discrepancy between its actual component characteristic signatures and those represented by the influence matrix of the new engine that is used for isolation.

Table 3.9. The composite diagnostic accuracy values obtained by applying the rules in Table 3.8 to the component degradation estimates associated with the results in Table 3.7

Engine Age	**Overall Accuracy**	**Diagnostic Accuracy**				
		Fan **DA_1**	LPC **DA_2**	HPC **DA_3**	HPT **DA_4**	LPT **DA_5**
new (0-cycle)	90%	10/10	10/10	10/10	10/10	5/10
1000-cycle	96%	10/10	10/10	10/10	10/10	9/10
2000-cycle	70%	10/10	10/10	1/10	8/10	6/10

3.4.2 An Illustrative Case

Consider the following hypothetical scenario, the current engine degradation is (Fan -1%, LPC -1%, HPC -1%, HPT 0%, LPT -1%), for which transient measurement data is collected from the engine. This data will be used as the baseline and compared to subsequent transient measurements collected from each subsequent flight. Consider next that the engine condition deteriorates one week later to (Fan -1%, LPC -1%, HPC -1%, HPT -2%, LPT -1%), which represents degradation of the HPT. The question is how DSIM will be used to alert the degradation of HPT in this case. In the absence of actual measurements from the engine, we considered the following health parameter values to depict the two above engine conditions:

$$\mathbf{\Theta} = \begin{bmatrix} 0.99 & 0.99 & 0.99 & 0.99 & 0.99 & 0.99 & 1.0 & 1.0 & 0.99 & 1.01 \end{bmatrix}^T$$

$$\text{for} \left(\text{Fan}: -1\% \quad \text{LPC}: -1\% \quad \text{HPC}: -1\% \quad \text{HPT}: 0\% \quad \text{LPT}: -1\% \right)$$

and

$$\mathbf{\Theta} = \begin{bmatrix} 0.99 & 0.99 & 0.99 & 0.99 & 0.99 & 0.99 & 0.98 & 1.02 & 0.99 & 1.01 \end{bmatrix}^T$$

$$\text{for} \left(\begin{array}{ccccc} \text{Fan}: -1\% & \text{LPC}: -1\% & \text{HPC}: -1\% & \text{HPT}: -2\% & \text{LPT}: -1\% \end{array} \right)$$

which represent the decrease in all the efficiencies and flow capacities by degradations, except for the flow capacities of turbines which increase with turbine degradations.

For application of DSIM, residuals were obtained, their output/parameter signatures were extracted by Gaussian smoothing, Gauss and Sombrero CWTs and then flagged according to Eq. (3.4) (computation time of 3.75 s on a PC). These flagged residuals were then mapped against the influence matrix of the engine, which has been obtained and archived for the new engine based on the parameter and component sensitivities of its outputs. The component degradation estimates according to both component and parameter sensitivities are shown in Table 3.10, which indicate that both sensitivities isolate the HPT as the degraded component.

Table 3.10. The composite component degradation estimates of the illustrative case using Gaussian smoothing, and the Gauss and Sombrero CWTs at the dominance factors of $\eta_d = 1.75$, $\eta_d = 2$ and $\eta_d = 2.25$ with the signature threshold size of $d = 5$

Source	**Component Degradation**				
	Fan	LPC	HPC	HPT	LPT
Actual	0	0	0	**1**	0
$\widehat{\mathbf{\Delta C}}_c$	0.1354	0.1925	0.2209	**0.2312**	0.2200
$\widehat{\mathbf{\Delta C}}_\theta$	0.1184	0.1434	0.2530	**0.2833**	0.2018

The above illustrative case is revealing of the potential utility of DSIM as a quick and effective means of component degradation monitoring in engines. Consider, for instance, the scenario where several measurement sets obtained from the previous cycles of the engine are chronologically ordered and used as baseline. With each baseline, all the subsequent measurements can be used to provide separate estimates of component degradations by DSIM. This then enables formation of chronological series of estimates which could inform the potential degradation of a component when component degradation estimates are consistently observed in the series.

3.4.3 Effect of Noise

In general, the outputs are low-pass filtered before being measured, and as such any jaggedness due to noise is often removed. Nevertheless, it is worthwhile examining the effect of noise on the diagnostic results. For this purpose, noise was added to the simulated outputs at the signal-to-noise ratio of SNR = [82, 94, 26, 45, 57, 23, 64] for individual outputs. For illustration purposes, the noisy residuals obtained for the 'illustrative case' are shown together with those obtained without noise in Fig. 3.4. By comparing the residual pairs, it is easy to see that while the noise effect is not as pronounced on the first two residuals, it completely distorts the shape of the last residual (P2.5), which is the smallest in size. This shape distortion then causes invalid flags and misdiagnosis. For illustration purposes, the component degradation estimates of the illustrative case obtained with noise contaminated outputs are shown in Table 3.11. The results clearly indicate the distortion by noise of the component degradation estimates, particularly those obtained by parameter sensitivities. Although the estimates by component sensitivities continue to match the actual degradation here, we consider it to be only accidental and not representative of superiority of component sensitivities in isolation.

Table 3.11. The composite component degradation estimates of the illustrative case with additive output noise

	Component Degradation				
	Fan	LPC	HPC	HPT	LPT
Actual	0	0	0	**1**	0
$\widehat{\mathbf{\Delta C}}_c$	0.1986	0.1613	0.2159	**0.2339**	0.1903
$\widehat{\mathbf{\Delta C}}_\theta$	**0.3251**	0.1314	0.2871	0.1218	0.1346

It is expected that additive output noise to be the most inhibitive factor in the performance of DSIM. As such, its practical implementation ought to be accompanied with rigorous time filtering and smoothing of the time measurements as well as denoising of the wavelet coefficients [2, 6, 25]. It was shown in previous work the effectiveness of compensa-

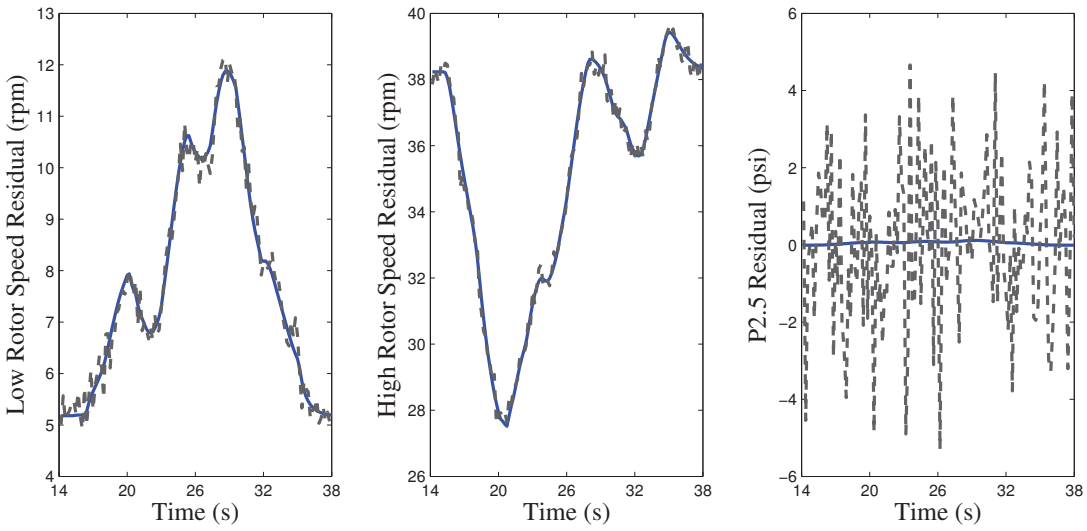

Figure 3.4. Sample residual counterparts of those in Fig. 3.1 with additive noise in the outputs

tion techniques in conjunction with output/parameter signatures [25] and believe similar techniques will be applicable in mitigating the effect of noise on residuals.

3.4.4 Effect of Flight Conditions

Another factor considered in this study is the effect of flight conditions on the estimation results. To study this factor, the illustrative case was repeated for the measurements separately obtained at the two different conditions of A:(20,000 ft altitude and 0.6 Mach speed) and B:(30,000 ft altitude and 0.7 Mach speed). Since in each of these cases, the output sensitivities differed considerably from those obtained at the initial flight condition of 0 altitude and 0 Mach speed, the influence matrices were obtained for each of the two flight conditions, using the value of 1 for all health parameters, to comply with the assumption of unknown health parameter values. The component degradation estimates obtained at each of these conditions are shown in Table 3.12. The results indicate that degradation estimates from component and parameter sensitivities differ for the first condition (20,000 ft and 0.6 Mach) but they are consistent for the second condition (30,000 ft and 0.7 Mach).

The explanation for the inaccurate estimates by the parameter sensitivities here lies in the highly correlated parameter sensitivities at this flight condition which render the influence matrices by the Gauss and Sombrero CWTs at different dominance factors rank-deficient. The uniqueness of the columns of influence matrices will be a consideration when selecting the flight conditions at which the data is to be collected.

Table 3.12. The composite degradation estimates of the illustrative case with additive output noise obtained by parameter and component sensitivities of the outputs

	Component degradation estimates				
	Fan	LPC	HPC	HPT	LPT
Actual =	[0	0	0	**1**	0]^T
			20,000 ft and 0.6 Mach		
$\widehat{\mathbf{\Delta C}}_c$ =	[0.1915	0.1855	0.2069	**0.2082**	0.2080]^T
$\widehat{\mathbf{\Delta C}}_\theta$ =	[0.2001	0.1993	**0.2072**	0.2052	0.1882]^T
			30,000 ft and 0.7 Mach		
$\widehat{\mathbf{\Delta C}}_c$ =	[0.1984	0.1961	0.2022	**0.2099**	0.1970]^T
$\widehat{\mathbf{\Delta C}}_\theta$ =	[0.1930	0.1826	0.2070	**0.2153**	0.2021]^T

3.4.5 Effect of Sensor Bias

Whereas DSIM is sensitive to measurement noise, it is immune to sensor bias, since it only considers the shape of the signal and is unaffected by shifts in the measurement magnitude. This point is illustrated in Fig. 3.5 for the residuals in Fig. 3.1 when random bias values are applied to the outputs. The plots clearly indicate the shapes to be identical while the magnitudes are shifted as the result of bias. As confirmation, diagnostic tests were performed on the biased residuals and found them to be identical to those obtained previously.

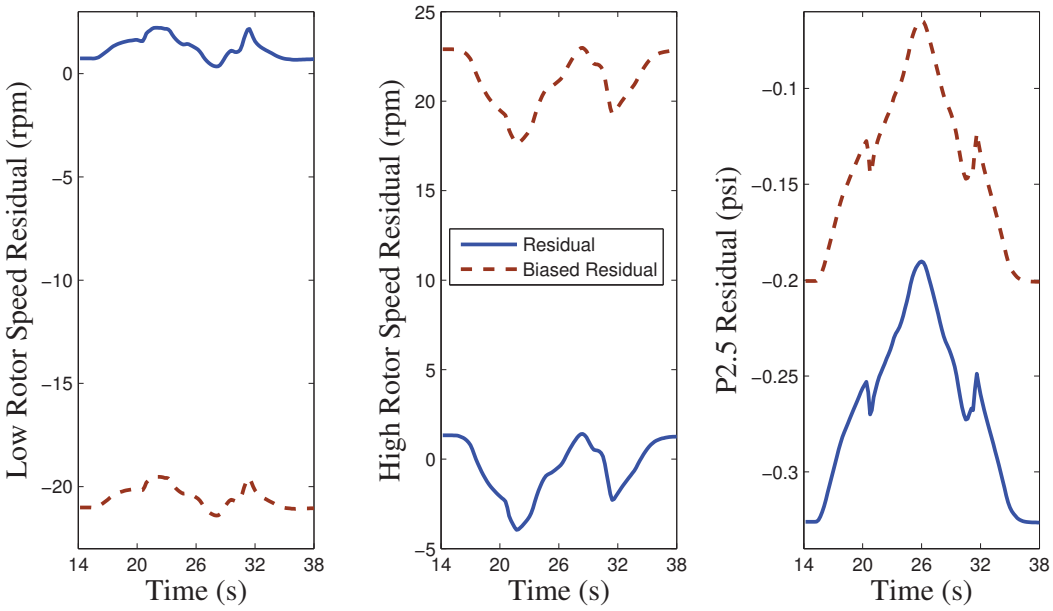

Figure 3.5. Sample residual counterparts of those in Fig. 3.1 obtained from biased sensory measurements

3.5 Discussion: Direct Method

The salient advantage of DSIM over the inverse approaches, such as nonlinear least-squares, is its independence from iterative function calls (i.e., simulation). DSIM is also favored among conventional direct methods, such as neural networks, for its independence from training. For its operation, DSIM compares the shapes of outputs, made available by CWT, with those obtained previously from the structure. Therefore, DSIM would need to (1) obtain the residuals by subtracting from the current sensory data the baseline data collected previously from the engine, (2) transform the residuals by Gaussian smoothing as well as the Gauss and Sombrero CWTs, (3) extract the residual signatures and flag them, and (4) map them against the influence matrix, available 'a priori' for damage localization. These steps take about 3 seconds on a regular PC. Given the minimal requirements demanded by DSIM, the results presented in this paper promise the beginning of a new

method of fault diagnosis to be developed for practical implementation. The issues that need to be considered for its practical application are:

- *Prior Computation:* In terms of its prior computation, DSIM method would require 11 'a priori' simulation runs of the engine model (given the 10 health parameters) to estimate the Jacobian, $\mathbf{\Phi}$, for the purpose of obtaining the influence matrix. Given the 20-second simulation runs of our engine model, this took about 4 minutes on a regular PC. The method would then transform, again 'a priori', the individual columns of $\mathbf{\Phi}$ into the time-scale domain by Gaussian smoothing as well as the Gauss and Sombrero CWTs for extracting the signatures and flagging them to render the influence matrix. This takes 20 seconds on a regular PC.

- *Modeling Accuracy:* The results reported in this thesis are simulation-based, whereas in practice the outputs will be measured from the engine. Given that the baseline outputs for the engine; i.e., y^n in Eq. (3.1), can be obtained from the engine itself and archived, the accuracy of the model is only critical to the derivation of the influence matrix. With the measured outputs available, a quick reality check for the model could be the agreement between the actual flagged residuals and those from simulation. Here, a promising anecdote that gives credence to the fidelity of the model is the success of the parameter estimation-based health monitoring methods; e.g., Kalman filters, that also rely on the fidelity of the model [21].

- *Excitation Input:* Two different excitation inputs were tested, of which the V-shaped input provides the more robust results across different output suites. Ideally, one would like DSIM to be independent of the excitation input, since the outputs are expected to be solely affected by component degradation. It was observed, however, that due to the nonlinearity of the engine, inputs vary in their effectiveness in accentuating component degradations. As such, the choice of excitation input is important

to the success of DSIM and the question remains if the transients produced during aircraft take-off will indeed be suitable for DSIM's application.

- *Noise:* As discussed earlier, DSIM is particularly sensitive to noise, since noise distorts the shape attributes of the outputs that need to be compared together for residual isolation. Since the purpose of this thesis is to illustrate the concept, no attempt is made at noise suppression. For its practical application, however, it will be necessary to study the effect of denoising techniques not only for removing measurement noise but also for eliminating degradation unrelated engine transients that could cause invalid residual flags.

- *Degradation Detection:* DSIM was evaluated with the expectation that a component degradation exists. In practice, it is unlikely that the residuals $\epsilon_j(t)$ will be nonzero due to noise even in the case of a non-degraded engine. Therefore the presence of degradation needs to be established as a precursor to degradation isolation. This is not a challenging task since such a detection mechanism can be established based on the size of the residuals or better yet according to deviations of individual output shapes from those archived for the engine.

- *Inclusion of Fault Diagnosis:* Another potential utility of the DSIM is in diagnosis for sudden faults. We consider this to be indeed a more simple task for DSIM than degradation isolation, since fault diagnosis can be readily performed by matching the flagged residuals with the fault signatures by, say, cosine similarities, as used with component sensitivities in Eq. (3.11). The only challenge for fault diagnosis is the ability to simulate the faults so as to be able to capture the fault signatures.

CHAPTER 4

THE INVERSE METHOD

Inverse methods in health monitoring and fault diagnosis, in general, use a model of the process and combine model outputs with measurements from the process to estimate performance degradation or damage. Examples of inverse methods include the Kalman filter, state observers and input observers.

The estimation of performance degradation via the inverse method as it applies to gas-turbine engines consists of estimation of the health parameters such as the component efficiencies and flow capacities. As such, the estimates effectively quantify the level of degradation and thereby complement the degradation isolation already provided by the direct method on-board (see Chapter 3). Current application of inverse methods in gas-turbine engine monitoring is performed exclusively post-flight based on steady-state measurements to accommodate on-board data acquisition. PARSIM, however, needs to use transient data due to its reliance on CWT. Of course, it should be noted that the use of transient data is not a unique capability of PARSIM - NLS can also be implemented on transient data. The advantage of the transient data is that it contains a broader spectrum of information, as compared to two or three steady-state data points taken during a typical flight.

Transparencies afforded in the time-scale domain enable PARSIM to hone in on the estimation of the heath parameters. Examples of such transparencies are the various shape attributes extracted from individual outputs by different CWTs, the separate estimate of individual parameter errors, and the quality of each parameter signature yielding the separate parameter error estimate. Preliminary results indicate that by taking advantage

of these transparencies PARSIM exhibits more favorable convergence characteristics even when faced with challenging local minima.

PARSIM has already been discussed in detail [3], so here only a brief presentation of it is provided to guide the reader to the extensions devised in this dissertation. Briefly, PARSIM capitalizes on the dominance of output sensitivities to decouple the prediction error in terms of individual model parameters for their separate estimation. There are several features of PARSIM that can be used for improved parameter estimation. One is its inherent uni-parameter estimation approach which allows for the adoption of separate adaptation step sizes, μ_i, for individual parameters. Second is the capacity of PARSIM to increase the amount of outputs available through multiple CWTs to represent its different shape attributes. Third is the ability to assess the accuracy of the parameter estimate by the quality of the corresponding parameter signature. This third feature, in turn, allows integration of the various estimates of each parameter obtained from different CWTs. It also allows adjustment of the adaptation step size according to the overall confidence attributed to each parameter estimate.

The above mentioned transparencies and degrees of freedom will be discussed and illustrated using three comparatively smaller yet challenging models, the Chua circuit, van der Pol oscillator and the non-linear mass-spring-damper prior to transitioning to health parameter estimation of the gas-turbine engine.

4.1 Parameter Error Estimation by PARSIM

Nonlinear dynamic models are the essential components of virtual environments that drive today's design, optimization, control, and automation practice. They provide the framework for characterizing the behavior of biological, ecological, social, and economic systems, as well as artifacts like aircraft and manufacturing systems. But to be effective, models must have a high degree of fidelity to reliably represent the process. This entails

having the correct form as well as accurate model parameters (coefficients and exponents). Effective parameter estimation, therefore, is essential to model development.

Dynamic models generally comprise a set of ordinary or partial differential equations and are often constructed according to first-principles or empirical knowledge of the system. Parameter estimation entails adjusting the model parameters, $\mathbf{\Theta} \in \Re^Q$, so as to minimize the sampled prediction error, $\epsilon(t_k, \mathbf{u}(t), \mathbf{\Theta})$ between the measured outputs $\mathbf{y}(t_k, \mathbf{u}(t)) = [y_1, \ldots, y_R]^T \in \Re^R$ and modeled outputs, $\hat{\mathbf{y}}(t_k, \mathbf{u}(t), \mathbf{\Theta}) = [\hat{y}_1, \ldots, \hat{y}_R]^T \in \Re^R$, obtained with the same input $\mathbf{u}(t)$, as [20]:

$$\epsilon(t_k, \mathbf{u}(t), \widehat{\mathbf{\Theta}}) = \mathbf{y}(t_k, \mathbf{u}(t)) - \hat{\mathbf{y}}(t_k, \mathbf{u}(t), \widehat{\mathbf{\Theta}}) \qquad t_k = t_1, \ldots, t_N \tag{4.1}$$

The parameter estimation problem can be viewed as a nonlinear optimization problem [1] wherein the solution is sought to minimize a cost function, V, in terms of the prediction error, as

$$\widehat{\mathbf{\Theta}}(\mathbf{u}(t), \epsilon^N) = \arg\min_{\mathbf{\Theta}} V(\mathbf{\Theta}, \mathbf{u}(t), \epsilon^N) \tag{4.2}$$

where $\epsilon^N \in \Re^{NR}$ for $t_k = t_1, \ldots, t_N$ denotes the vector of sampled prediction error.

The solution to the above optimization problem can be sought by gradient-based methods such as nonlinear least-squares (NLS) [33], or genetic algorithms [15], convex programming [14], Monte Carlo optimization [31], or adaptive estimation techniques [18, 30, 32]. Regardless of the solution method used, the cost function V in Eq. (4.2) is generally formulated based on the magnitude of the prediction error, as

$$V(\mathbf{\Theta}, \mathbf{u}(t), \epsilon^N) = \sum_{k,j}^{N,R} L(\epsilon_j(t_k)) \tag{4.3}$$

where L is a scalar-valued (typically positive) function such as the square function used in NLS.

Among the above optimization methods, NLS is the method of choice for dynamic systems due to its efficient use of gradients. It adjusts the model parameters iteratively as

$$\widehat{\mathbf{\Theta}}(q+1) = \widehat{\mathbf{\Theta}}(q) + \mu\widehat{\mathbf{\Delta\Theta}}(q) \tag{4.4}$$

where q is the iteration number, $\mathbf{\Delta\Theta} = \mathbf{\Theta}^* - \widehat{\mathbf{\Theta}} = [\Delta\theta_1, \ldots, \Delta\theta_Q]^T$ denotes the vector of parameter errors between the true parameter values $\mathbf{\Theta}^* = [\theta_1^*, \ldots, \theta_Q^*]^T \in \mathcal{R}^Q$ and their current estimate $\widehat{\mathbf{\Theta}} = [\widehat{\theta}_1, \ldots, \widehat{\theta}_Q]^T$. The vector of parameter errors is estimated at each iteration by NLS as

$$\widehat{\mathbf{\Delta\Theta}} = (\mathbf{\Phi}^T\mathbf{\Phi})^{-1}\mathbf{\Phi}^T\epsilon^N \tag{4.5}$$

where $\mathbf{\Phi} \in \Re^{NR\times Q}$ denotes the matrix of output sensitivities (i.e., Jacobian), having the form

$$\mathbf{\Phi} = \begin{bmatrix} \partial\hat{y}_1(t_1,\widehat{\mathbf{\Theta}})/\partial\theta_1 & \ldots & \partial\hat{y}_1(t_1,\widehat{\mathbf{\Theta}})/\partial\theta_Q \\ \vdots & \ddots & \vdots \\ \partial\hat{y}_1(t_N,\widehat{\mathbf{\Theta}})/\partial\theta_1 & \ldots & \partial\hat{y}_1(t_N,\widehat{\mathbf{\Theta}})/\partial\theta_Q \\ \vdots & \ddots & \vdots \\ \partial\hat{y}_R(t_1,\widehat{\mathbf{\Theta}})/\partial\theta_1 & \ldots & \partial\hat{y}_R(t_1,\widehat{\mathbf{\Theta}})/\partial\theta_Q \\ \vdots & \ddots & \vdots \\ \partial\hat{y}_R(t_N,\widehat{\mathbf{\Theta}})/\partial\theta_1 & \ldots & \partial\hat{y}_R(t_N,\widehat{\mathbf{\Theta}})/\partial\theta_Q \end{bmatrix} \tag{4.6}$$

with each column characterizing the sensitivity of all outputs to an individual model parameter at $t_k = t_1, \ldots, t_N$.

The NLS solution implemented in Eq. (4.5) is based on the magnitude of the prediction error, as defined by the cost function in Eq. (4.3). An appealing alternative to the error magnitude is the error shape (e.g., slope and/or rate of slope change), as represented by the continuous wavelet transform(s) (CWT)(s) [23] of the prediction error. However, the CWTs of time series span both times and scales. They convert an NR dimensional time series into R surfaces spanning the time-scale planes of $N \times M$ dimension, hence they

expand Mfold the size of the data to be used for parameter estimation. This increased dimensionality, in turn, impedes the direct insertion of the data contained in these surfaces in Eq. (4.5) for parameter estimation, because the resulting $\mathbf{\Phi}$ and ϵ^N which represent the cascaded elements of these surfaces would be too bloated to be implemented in Eq. (4.5). This dissertation offers a methodical solution to this data expansion by adopting a selective approach to data inclusion.

The salient feature of the proposed method is its size mitigation of the CWT surfaces by focusing on isolated information-rich regions of these surfaces. These regions of the time-scale plane, called 'parameter signatures', can be isolated because of the enhanced delineation of time series in the time-scale domain. Each region is sought wherein the sensitivity of an output to a model parameter dominates its sensitivities to all the other model parameters, hence making it possible to attribute the prediction error to the error of individual model parameters in their corresponding parameter signature [3]. These single-parameter approximations of the prediction error enable, in turn, consideration of isolated segments of surfaces of the output sensitivities and prediction error for parameter estimation, thus making it tractable to include isolated portions of the CWTs in Eq. (4.5) for parameter estimation. A potential pitfall of the above scheme is the absence of parameter signatures due to parameter non-identifiability. For such cases, an alternative integration routine is considered wherein separate estimates of individual model parameters are obtained for their iterative adaptation.

4.2 Overview of PARSIM

The single-output single-WT separate parameter estimation solution of PARSIM is presented in [3]. Here its generalized solutions are provide that can accommodate multiple outputs and multiple CWTs. Briefly, PARSIM capitalizes on the enhanced delineation of output sensitivities to isolate regions of the time-scale plane wherein one output sensitivity

dominates all the others. Justified by this dominance, the prediction error is attributed to the error of the corresponding parameter in each region, hence allowing inclusion of select portions of wavelet coefficients for least-squares estimation or separate estimation of individual parameter errors.

PARSIM, like NLS, assumes an accurate and identifiable model, M_{Θ}. This implies that the true model parameter values $\mathbf{\Theta}^*$ can be found if the model outputs $\hat{\mathbf{y}}(t)$ obtained under the same input $\mathbf{u}(t)$ applied to the process match the observations $\mathbf{y}(t)$ in the mean square sense; i.e.,

$$\mathbf{y}(t, \mathbf{u}(t)) \equiv \hat{\mathbf{y}}(t, \mathbf{u}(t), \mathbf{\Theta}) \Longrightarrow \mathbf{\Theta} = \mathbf{\Theta}^* \tag{4.7}$$

PARSIM, like NLS, also relies on a first-order approximation of the model as

$$\mathbf{y}(t, \mathbf{u}(t)) \approx \hat{\mathbf{y}}(t, \mathbf{u}(t), \widehat{\mathbf{\Theta}}) + \sum_{i=1}^{Q} \Delta\theta_i \left. \frac{\partial \hat{\mathbf{y}}(t, \mathbf{u}(t), \mathbf{\Theta})}{\partial \theta_i} \right|_{\mathbf{\Theta}=\widehat{\mathbf{\Theta}}} + \nu \tag{4.8}$$

to yield the approximation of the prediction error, as

$$\epsilon(t, \mathbf{u}(t), \mathbf{\Theta}^*, \widehat{\mathbf{\Theta}}) \approx \mathbf{\Phi}\widehat{\Delta\mathbf{\Theta}} + \nu \tag{4.9}$$

where ν denotes measurement noise.

4.2.1 Notion of Parameter Signature

The enhanced delineation of output sensitivities enables isolation of regions of the time-scale domain wherein a single output sensitivity dominates the others [3]. Each such region is referred to as a *parameter signature*, as defined formally below.

Definition 4: The parameter signature $\Gamma_{i,j}^r$ of the parameter θ_i is the region consisting of all pixels (t_k, s_l) in the time-scale plane wherein the normalized wavelet coefficients of the corresponding output sensitivity $\left|\overline{W_r\{\partial \hat{y}_j / \partial \theta_i\}}(t_k, s_l)\right|$ exceeds the normalized wavelet

coefficients of all the other output sensitivities by a dominance factor η_j^r, expressed mathematically as

$$\begin{aligned} \text{If } \exists(t_k, s_l) \ \ni \left|\overline{W_r\{\partial\hat{y}_j/\partial\theta_i\}}(t_k, s_l)\right| \quad &> \quad \eta_j^r \left|\overline{W_r\{\partial\hat{y}_j/\partial\theta_m\}}(t_k, s_l)\right| \\ \forall\, m = 1, \ldots, Q \neq i \quad &\Longrightarrow \quad (t_k, s_l) = (t_k^i, s_l^i) \in \Gamma_{i,j}^r \end{aligned} \tag{4.10}$$

where j is associated with the output, the subscript or superscript r denotes the type of CWT (i.e., Gauss, Sombrero, etc.) and

$$\overline{W_r\{\partial\hat{y}_j/\partial\theta_i\}} = \frac{W_r\{\partial\hat{y}_j/\partial\theta_i\}}{\max_{(t,s)} |W_r\{\partial\hat{y}_j/\partial\theta_i\}|} \tag{4.11}$$

Now if the dominance factor η_j^r is selected to be large; i.e., $\eta_j^r >> 1$, then one can assume the wavelet coefficients of the corresponding output sensitivity, $\partial\hat{y}_j/\partial\theta_i$, to be dominant among the wavelet coefficients of the output sensitivities associated with output y_j. This then enables us to redefine the wavelet coefficient of the prediction error in Eq. (4.9) in terms of a single parameter at the corresponding parameter signature $\Gamma_{i,j}^r$, as

$$W_r\{\epsilon_j\}(t_k^i, s_l^i) \approx \Delta\theta_i \, W_r\{\partial\hat{y}_j/\partial\theta_i\}(t_k^i, s_l^i) + W_r\{\nu\} \qquad \forall\, (t_k^i, s_l^i) \in \Gamma_{i,j}^r \tag{4.12}$$

For illustration purposes, the parameter signatures of two different parameters are shown by the grey regions of the time-scale plane in Fig. 4.1 against the CWT (surface) of the prediction error. According to Eq. (4.12), the prediction error at each grey pixel (i.e., pixel of parameter signature) can be attributed to the error of the corresponding parameter, $\Delta\theta_i$, and used for its estimation. Ideally, each of the parameter error estimates $\widehat{\Delta\theta}_i$, at each pixel $(t_k^i, s_l^i) \in \Gamma_{i,j}^r$, should be identical with a perfect parameter signature. But as is shown

in [3] and subsequent sections, the parameter signatures are far from perfect and, as such, the parameter error estimates at different pixels are not identical. We addressed this in [3] for a single WT by obtaining the mean estimate of the parameter error over all pixels of the corresponding parameter signature. However, here multiple parameter signatures obtained from different CWTs of various outputs are being encountered . As such, a more elaborate solution needs to be formulated wherein the transparencies afforded by the parameter signatures can be used to advantage. Two solutions have been developed to consolidate the parameter estimates obtained from the above single-parameter approximation of the prediction error in Eq. (4.12). The first solution adopts a least-squares approach to the integration of estimates. The second solution is an alternate approach when the absence of parameter signatures, due to low parameter identifiability, impedes the application of the preferred least-squares solution.

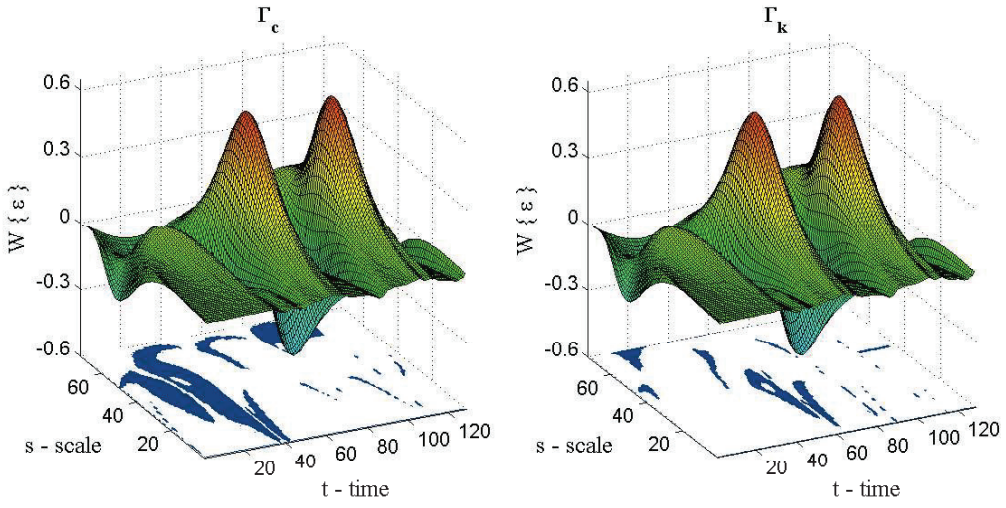

Figure 4.1. Gauss wavelet coefficients of the prediction error shown as a surface together with the parameter signatures of two model parameters shown by grey regions in the time-scale plane

4.2.2 The Least-Squares Solution

PARSIM uses a format akin to NLS for integration of the parameter error estimates, with the form

$$\widehat{\mathbf{\Delta\Theta}}_s = (\mathbf{\Phi_s}^T\mathbf{\Phi_s})^{-1}\mathbf{\Phi_s}^T\epsilon_s \tag{4.13}$$

where $\mathbf{\Phi_s}$ is the matrix of wavelet coefficients of output sensitivities at the parameter signatures, and ϵ_s is the matrix of wavelet coefficients of the prediction error at the parameter signatures. Therefore, the noted feature of PARSIM is its selective incorporation of wavelet coefficients in the least-squares solution in accordance with the decoupled prediction error formulation in Eq. (4.12). Using this format, the Jacobian matrix, $\mathbf{\Phi_s}$, finds the form

$$\mathbf{\Phi_s} = \begin{pmatrix} W_1\{\partial y_1/\partial\theta_1\}|_{\Gamma^1_{1,1}} & W_1\{\partial y_1/\partial\theta_2\}|_{\Gamma^1_{2,1}} & \dots & W_1\{\partial y_1/\partial\theta_Q\}|_{\Gamma^1_{Q,1}} \\ \vdots & \vdots & \ddots & \vdots \\ W_1\{\partial y_1/\partial\theta_1\}|_{\Gamma^1_{1,1}} & W_1\{\partial y_1/\partial\theta_2\}|_{\Gamma^1_{2,1}} & \dots & W_1\{\partial y_1/\partial\theta_Q\}|_{\Gamma^1_{Q,1}} \\ W_1\{\partial y_2/\partial\theta_1\}|_{\Gamma^1_{1,2}} & W_1\{\partial y_2/\partial\theta_2\}|_{\Gamma^1_{2,2}} & \dots & W_1\{\partial y_2/\partial\theta_Q\}|_{\Gamma^1_{Q,2}} \\ \vdots & \vdots & \ddots & \vdots \\ W_1\{\partial y_2/\partial\theta_1\}|_{\Gamma^1_{1,2}} & W_1\{\partial y_2/\partial\theta_2\}|_{\Gamma^1_{2,2}} & \dots & W_1\{\partial y_2/\partial\theta_Q\}|_{\Gamma^1_{Q,2}} \\ \vdots & \vdots & \ddots & \vdots \\ W_P\{\partial y_R/\partial\theta_1\}|_{\Gamma^P_{1,R}} & W_P\{\partial y_R/\partial\theta_2\}|_{\Gamma^P_{2,R}} & \dots & W_P\{\partial y_R/\partial\theta_Q\}|_{\Gamma^P_{Q,R}} \\ \vdots & \vdots & \ddots & \vdots \\ W_P\{\partial y_R/\partial\theta_1\}|_{\Gamma^P_{1,R}} & W_P\{\partial y_R/\partial\theta_2\}|_{\Gamma^P_{2,R}} & \dots & W_P\{\partial y_R/\partial\theta_Q\}|_{\Gamma^P_{Q,R}} \end{pmatrix} \tag{4.14}$$

where each column comprises the cascaded wavelet coefficients, by various CWTs, of the outputs sensitivities of a parameter at its parameter signatures. By confining the wavelet coefficients to those at the parameter signatures, PARSIM reduces the size of the Jacobian from $\Re^{NMR\times Q}$ to $\Re^{\max(\#_{r,j})R\times Q}$ where the dimension $\max(\#_{r,j})$ denotes the maximum cardinal number of the parameter signatures for all θ_i at the rth CWT and jth output. It is

worth noting here that the size of the parameter signatures are uniformized by padding the wavelet coefficients of size-deficient parameter signatures, relative to $\max(\#_{r,j})$, with zero.

The least-squares formulation of Eq. (4.13) also deviates from the ordinary least-squares formulation of Eq. (4.5) in that it requires the prediction error to be defined as a matrix, of the form

$$\epsilon_s = \begin{pmatrix} W_1\{\epsilon_{y_1}\}|_{\Gamma^1_{1,1}} & W_1\{\epsilon_{y_1}\}|_{\Gamma^1_{2,1}} & \dots & W_1\{\epsilon_{y_1}\}|_{\Gamma^1_{Q,1}} \\ \vdots & \vdots & \ddots & \vdots \\ W_1\{\epsilon_{y_1}\}|_{\Gamma^1_{1,1}} & W_1\{\epsilon_{y_1}\}|_{\Gamma^1_{2,1}} & \dots & W_1\{\epsilon_{y_1}\}|_{\Gamma_{Q,1}} \\ W_1\{\epsilon_{y_2}\}|_{\Gamma^1_{1,2}} & W_1\{\epsilon_{y_2}\}|_{\Gamma^1_{2,2}} & \dots & W_1\{\epsilon_{y_2}\}|_{\Gamma^1_{Q,2}} \\ \vdots & \vdots & \ddots & \vdots \\ W_1\{\epsilon_{y_2}\}|_{\Gamma^1_{1,2}} & W_1\{\epsilon_{y_2}\}|_{\Gamma^1_{2,2}} & \dots & W_1\{\epsilon_{y_2}\}|_{\Gamma^1_{Q,2}} \\ \vdots & \vdots & \ddots & \vdots \\ W_P\{\epsilon_{y_R}\}|_{\Gamma^P_{1,R}} & W_P\{\epsilon_{y_R}\}|_{\Gamma^P_{2,R}} & \dots & W_P\{\epsilon_{y_R}\}|_{\Gamma^P_{Q,R}} \\ \vdots & \vdots & \ddots & \vdots \\ W_P\{\epsilon_{y_R}\}|_{\Gamma^P_{1,R}} & W_P\{\epsilon_{y_R}\}|_{\Gamma^P_{2,R}} & \dots & W_P\{\epsilon_{y_R}\}|_{\Gamma^P_{Q,R}} \end{pmatrix} \tag{4.15}$$

where the ith column of the error matrix, ϵ_s, comprises the cascaded wavelet coefficients, by various CWTs, of the prediction errors of different outputs at the corresponding parameter signatures $\Gamma^r_{i,j}$ of parameter θ_i. Based on the above formulation, the parameter error estimate, $\widehat{\mathbf{\Delta\Theta_s}}$, according to Eq. (4.13) will be a $Q \times Q$ matrix of the form

$$\widehat{\mathbf{\Delta\Theta_s}} = \begin{pmatrix} \widehat{\Delta\theta_1} & \zeta_{(1,2)} & \dots & \zeta_{(1,Q)} \\ \zeta_{(1,2)} & \widehat{\Delta\theta_2} & \dots & \zeta_{(2,Q)} \\ \vdots & \vdots & \ddots & \\ \zeta_{(1,R)} & \dots & \zeta_{(R,Q-1)} & \widehat{\Delta\theta_Q} \end{pmatrix} \tag{4.16}$$

where each column of $\widehat{\mathbf{\Delta\Theta_s}}$ is obtained by least-squares estimation using the corresponding column in ϵ_s. Among the components of $\widehat{\mathbf{\Delta\Theta_s}}$, we only consider the diagonal terms, $\widehat{\Delta\theta}_i$, which are obtained using the components of $\mathbf{\Phi_s}(.,i)$ and $\epsilon_s(.,i)$ associated with the same parameter signatures, hence, representing a true adaptation of the least-squares method. The off-diagonal terms, $\zeta_{(a,b)}$, by the same analogy, are meaningless in that they are obtained from components of $\mathbf{\Phi_s}(.,a)$ and $\epsilon_s(.,b)$ that relate to different parameter signatures. The parameter error estimates $\widehat{\Delta\theta}_i$ are then updated as in NLS

$$\widehat{\theta}_i(q+1) = \widehat{\theta}_i(q) + \mu_i(q)\widehat{\Delta\theta}_i(q) \tag{4.17}$$

except that here each parameter is adapted separately with its separate adaptation step size $\mu_i(q)$.

As will be shown later, the above solution is effective except in cases where no parameter signature can be obtained for a parameter across different CWTs of various outputs. In such cases, the Jacobian $\mathbf{\Phi_s}$ would be rank deficient, precluding the implementation of the least-squares solution. Lack of a signature can be due to a variety of causes. One is when the parameter is not observable through any of the outputs. Another is when an output sensitivity is closely correlated to another output sensitivity such that no wavelet coefficient from a CWT dominates those of the others. A scenario wherein parameter signatures cannot be extracted is illustrated in the context of the Chua's circuit (Platform 1), described below.

Platform 1: Chua's circuit is described by the ordinary differential equations [19]:

$$\begin{aligned}
\frac{dI_3}{dt} &= -\frac{R_0}{L}I_3 - \frac{1}{L}V_2 \\
\frac{dV_2}{dt} &= \frac{1}{C_2}I_3 - \frac{G}{C_2}(V_2 - V_1) \\
\frac{dV_1}{dt} &= \frac{G}{C_1}(V_2 - V_1) - \frac{1}{C_1}f(V_1)
\end{aligned}$$

$$\mathbf{y} \;=\; \left[\; I_3 \quad V_2 \quad V_1 \;\right]^T \tag{4.18}$$

where

$$f(V_1) = G_b V_1 - (G_a - G_b)(|V_1 + E| - |V_1 - E|)$$

and

$$\mathbf{\Theta}^* = \left[\; L^* \quad R_0^* \quad C_2^* \quad G^* \quad C_1^* \;\right]^T = \left[\; -9.7136 \quad 4.75 \quad -1.0837 \quad 33.932813 \quad 1 \;\right]^T$$

To avoid the chaotic aspect of Chua's circuit, a short time window of 5 seconds is considered for simulation. The error surfaces of Chua's circuit from different outputs in this time window are devoid of local minima but have shallow gradients which pose challenging parameter identifiability conditions. The parameters G_a^*, G_b^* and E^* are non-identifiable by any of the outputs, so are held constant at their true values. For this illustration and throughout the thesis for this model, the nominal parameter values, which are also used as the initial values of the parameters for their estimation, are

$$\bar{\mathbf{\Theta}} = \left[\; 0.95L^* \quad 1.05R_0^* \quad 0.95C_2^* \quad 1.05G^* \quad 0.95C_1^* \;\right]^T$$

The prediction error $\epsilon(t) = \hat{\mathbf{y}}(t, \mathbf{\Theta}^*) - \hat{\mathbf{y}}(t, \bar{\mathbf{\Theta}})$ then reflects the mismatch between the true and nominal parameter values.

The lack of parameter signatures due to parameter non-identifiability is illustrated for an episode of Chua's circuit in Table 4.1. Listed in this table are the number of pixels (cardinal number) of the parameter signatures from three different transformations (Gaussian smoothing, Gauss and Sombrero CWTs) of the first two outputs. The absence of parameter signatures is clear from the zeros in the last column. This inability to extract parameter signatures, at this episode of parameter estimation, results in a rank-deficient Jacobian $\mathbf{\Phi_s}$, with a nill column, and unfit for parameter estimation. In order to remedy disruptions to parameter estimation by rank-deficient Jacobians, a second estimation procedure is developed for PARSIM as discussed next.

Table 4.1. Number of pixels of parameter signatures from three different transformations (Gaussian smoothing and Gauss and Sombrero CWTs) of the first two outputs (I_3 and V_2) of the Chua's circuit

WT	**Parameter Signature Size**				
	$\widehat{\Delta L}$	$\widehat{\Delta R_0}$	$\widehat{\Delta C_2}$	$\widehat{\Delta G}$	$\widehat{\Delta C_1}$
CWT_1^1	93	759	0	0	0
CWT_2^1	789	57	0	2	0
CWT_1^2	0	970	9	176	0
CWT_2^2	906	0	20	3	0
CWT_1^3	1487	1272	0	0	0
CWT_2^3	199	0	0	19	0

4.2.3 The Separate Parameter Estimate Solution

A direct ramification of the single-parameter approximation of the prediction error in Eq. (4.12) is that the error of the corresponding parameter, $\Delta\theta_i$, can be estimated at the pixels (t_k^i, s_l^i) of the associated parameter signature $\Gamma_{i,j}^r$. Ideally the estimate of $\Delta\theta_i$ at a pixel of $\Gamma_{i,j}^r$ should be identical to the next at another pixel. However, the parameter signatures are not perfect and, as such, the parameter error estimates are not identical. In the single-WT single-output implementation of PARSIM [3], the mean of the parameter error estimates obtained at the individual pixels of the parameter signature were used in Eq. (4.17), as

$$\widehat{\Delta\theta}_{i,j}^r = \overline{\Delta\theta}_{i,j}^r = \frac{1}{N_{i,j}^r} \sum_{k,l}^{N,M} \frac{W_r\{\epsilon_j\}(t_k^i, s_l^i)}{W_r\{\partial\hat{y}_j/\partial\theta_i\}(t_k^i, s_l^i)} \;\; \forall\, (t_k^i, s_l^i) \in \Gamma_{i,j}^r \tag{4.19}$$

where $N_{i,j}^r$ denotes the number of pixels (t_k^i, s_l^i) included in $\Gamma_{i,j}^r$ (i.e., its cardinal number). In the multi-CWT multi-output implementation of PARSIM, however, several $(P \times R)$ estimates are obtained, each different from the other, as shown in Table 4.2 at an estimation iteration of Chua's circuit parameters. As expected, the estimates vary widely, some being in even opposite direction (e.g., those of ΔG). One could use, here, the averaging strategy adopted in [3] again, but such a strategy would not only render too crude an estimate but

also disregard the quality of the parameter signatures yielding the individual estimates. A more prudent approach, therefore, is to consider a weighted strategy for the integration of the estimates whereby the accuracy of each estimate is inferred from the quality of the associated parameter signature. Such a strategy will have the form

$$\widehat{\Delta\theta}_i = \sum_{r,j}^{P,R} w_{i,j}^r \widehat{\Delta\theta}_{i,j}^r \tag{4.20}$$

where $w_{i,j}^r$ denotes the weight assigned to each estimate $\widehat{\Delta\theta}_{i,j}^r$ according to the confidence in its accuracy. It is shown below that the weights $w_{i,j}^r$ can be defined in terms of the quality of the parameter signatures, which can be obtained according to the transparencies afforded in the time-scale domain.

Table 4.2. Sample of parameter error estimates obtained from two CWTs (Gauss and Sombrero) of the three Chua's circuit outputs, shown with their true values

Parameter	**True Error**	**Error Estimates**					
		CWT_1^1	CWT_2^1	CWT_3^1	CWT_1^2	CWT_2^2	CWT_3^2
$\widehat{\Delta L}$	-0.48	-0.32	-0.58	-0.88	-0.49	-0.37	-0.38
$\widehat{\Delta R_0}$	-0.23	0.079	0.071	0.069	0.0	0.002	0.052
$\widehat{\Delta C_2}$	-0.05	0.0	-0.009	-0.0108	-0.0118	0.0	-0.0115
$\widehat{\Delta G}$	-1.69	0.67	-2.17	1.16	-1.13	-0.915	-4.65
$\widehat{\Delta C_1}$	0.05	0.0	0.0	0.0	0.005	0.0	0.0

As implied above, there are measures available to PARSIM to assess the quality of the parameter signatures. At the same time, PARSIM can benefit from several degrees of freedom to affect the quality of parameter signatures for improved estimation. One such degree of freedom is that several wavelet transforms can be obtained for each output to characterize its different shape attributes. A second degree of freedom is the dominance factor η_j^r in Eq. (4.10) used for parameter signature extraction. A third degree of freedom is the adaptation step size, $\mu_i(q)$ in Eq. (4.17), that can be adjusted at each iteration based on

the quality of the corresponding parameter error estimate. PARSIM uses the transparencies afforded in the time-scale domain to assess the quality of parameter signatures. It then uses its degrees of freedom to affect the parameter signatures quality and the parameter estimates they provide. The transparencies used for assessing the parameter signature quality are discussed next, followed by a description of the degrees of freedom PARSIM uses to affect the quality of parameter signatures.

4.3 Transparencies of PARSIM

The transparencies used by PARSIM to evaluate the quality of parameter estimates correspond to the consistency of the parameter error estimates across the pixels of the parameter signature, as depicted in the right-hand side of Eq. (4.19). The inconsistency of the parameter error estimates arises from not only the first-order approximation of the prediction error in Eq. (4.7) but also the approximate nature of parameter signatures, stemming from the finite dominance factor η_j^r used in Eq. (4.10) that does not necessarily satisfy the requisite condition $\eta_j^r >> 1$ for Eq. (4.12). This inconsistency (non-uniformity) of the parameter error estimates provides the basis for evaluating the quality of the parameter signatures through measures such as entropy, variance and unidirectionality of the parameter error estimates. Entropy represents the information content of the parameter error estimates. The variance of the estimates represents their level of dispersion across the parameter signature. Their unidirectionality informs the uniformity of the parameter error estimates in direction (sign). First discussed will be the measures that elucidate these transparencies and then explain how they are used in affecting parameter estimation by PARSIM, through manipulating its degrees of freedom (in Section 4.4).

4.3.1 Entropy

A common measure of information content or complexity of information of a population (set) is the Shannon entropy. In this case, the population comprises the parameter error

estimates, $\widehat{\Delta\theta}^{r}_{i,j}$, obtained at individual pixels of the parameter signature $\Gamma^{r}_{i,j}$, as formulated in Eq. (4.19). The Shannon entropy $S^{r}_{i,j}$ of the parameter error estimates is obtained as

$$S^{r}_{i,j} = \sum_{k,l}^{N,M} \bar{W}\{\widehat{\Delta\theta}^{r}_{i,j}\}^2(t^i_k, s^i_l) \log(\bar{W}\{\widehat{\Delta\theta}^{r}_{i,j}\}^2(t^i_k, s^i_l)) \qquad \forall\, (t^i_k, s^i_l) \in \Gamma^{r}_{i,j} \tag{4.21}$$

where

$$\bar{W}\{\Delta\theta^{r}_{i,j}\}^2(t^i_k, s^i_l) = \frac{W\{\Delta\theta^{r}_{i,j}\}^2(t^i_k, s^i_l)}{\sum_k \sum_l W\{\Delta\theta^{r}_{i,j}\}^2(t^i_k, s^i_l)} \tag{4.22}$$

Higher entropies represent more evenly distributed parameter error estimates across the pixels of the corresponding parameter signature. By the same token, the more concentrated the parameter error estimates the lower is the entropy of their population. In accordance with this concept, minimum entropy corresponds to the bulk of the information content centered at as few pixels as possible in the parameter signature, leading to enhanced separation of the columns of the Jacobian $\mathbf{\Phi_s}$ in Eq. (4.14). Entropy will serve as the measure of parameter signature quality and select η^{r}_{j} in Eq. (4.10) to achieve minimum entropy.

4.3.2 Variance

Variance and entropy are equivalent measures for binary normally distributed populations [12]. However, for non-binary populations, entropy represents the information content, whereas variance emphasizes the overall distance of the elements from their mean value. Since variance provides a higher level of resolution for the scatter of the parameter error estimates about their mean, it is found to be a better measure of confidence in the fidelity of the parameter error estimates. This point is illustrated in Fig. 4.2 via two sets of parameter error estimates. Even though the two sets of parameter error estimates have almost the same entropies, the left set has a much larger variance, representing the higher level of scatter relative to the right set. The variance of the estimates will be used, computed as

$$\gamma^{r}_{i,j} = \frac{1}{N^{r}_{i,j} - 1} \sum_{k,l}^{N,M} \left(\frac{W_r\{\epsilon_j\}(t^i_k, s^i_l)}{W_r\{\frac{\partial y_j}{\partial \theta_i}\}(t^i_k, s^i_l)} - \overline{\Delta\theta}^{r}_{i,j} \right)^2 \quad \forall\, (t^i_k, s^i_l) \in \Gamma^{r}_{i,j} \tag{4.23}$$

to adjust the adaptation step size $\mu_i(q)$ in Eq. (4.17), where $\overline{\Delta\theta}^r_{i,j}$ represents the mean of the parameter error estimates across the parameter signature, as computed in Eq. (4.19).

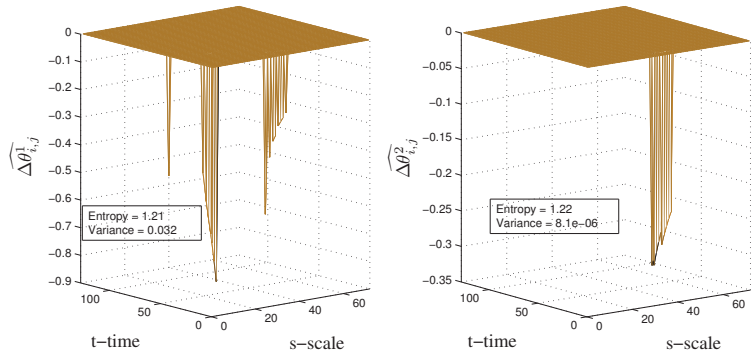

Figure 4.2. Illustration of the higher resolution provided by variance vis-*à*-vis entropy in representing the scatter of the parameter error estimates

4.3.3 Unidirectionality

It will commonly happen that the elements of the parameter error estimate $\widehat{\Delta\theta}^r_{i,j}$ at individual pixels of the parameter signature (t^i_k, s^i_l) will be nonuniform in their directionality (sign). As such, they contradict each other over the sign of the parameter error and reflect negatively on the quality of the parameter signature and the estimate it yields. The unidirectionality of the parameter error estimate, $d^r_{i,j}$, is defined as the percentage of unanimity in the signs of the parameter error estimates, and compute it as

$$d^r_{i,j} = \frac{\sum_{k,l}^{N,M} sgn\left(\widehat{\Delta\theta}^r_{i,j}(t^i_k, s^i_l)\right)}{N^r_{i,j}} \qquad \forall\,(t^i_k, s^i_l) \in \Gamma^r_{i,j} \tag{4.24}$$

where 'sgn' denotes the sign of the parameter error estimate $\widehat{\Delta\theta}^r_{i,j}(t^i_k, s^i_l)$ represented by +1 or -1, and $N^r_{i,j}$ represents the number of pixels (t^i_k, s^i_l) included in the parameter signature $\Gamma^r_{i,j}$. According to the above formula, a value of +1 or -1 for $d^r_{i,j}$ indicates uniformity of direction for all the parameter error estimates. At the other extreme, a value of zero would indicate an equal number of positive and negative estimates, reflecting negatively

on the quality of the parameter error estimates. This point is illustrated by the two sets of parameter error estimates in Fig. 4.3. While the entropy of both sets are close to each other, the estimates from the left parameter signature are unidirectional, with a unidirectionality of 1, whereas those from the right parameter signature are conflicting with a unidirectionality of 0.48. We will use the unidirectionality value as a factor in determining the adaptation step size $\mu_i(q)$ in Eq. (4.17).

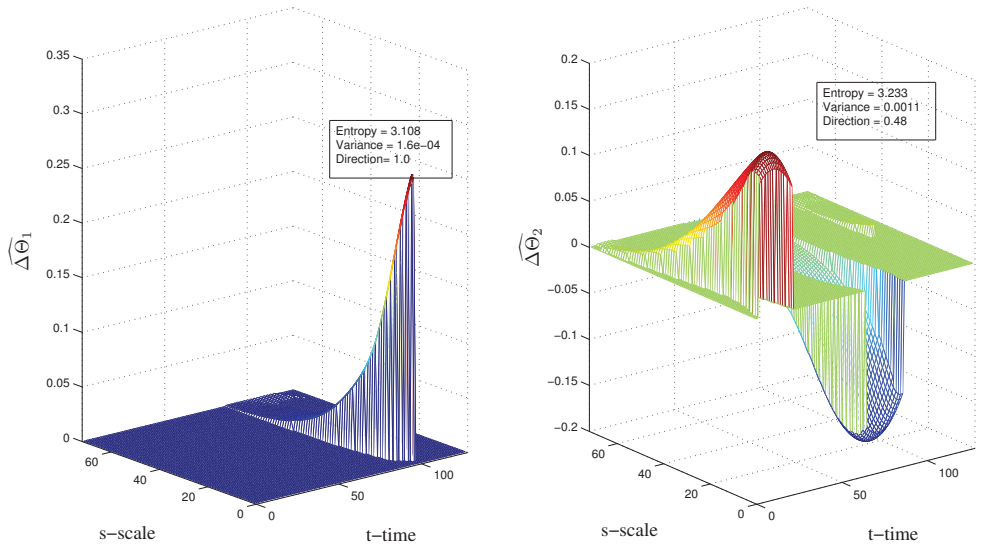

Figure 4.3. Illustration of the significance of unidirectionality vis-*à*-vis variance and entropy in representing the uniformity of the parameter error estimates

4.4 Degrees of Freedom of PARSIM

The above-mentioned transparencies will be used as feedback to adjust several degrees of freedom available to PARSIM for improving its parameter estimation performance. One such degree of freedom is constricting the size of the parameter signatures so that only pixels closest in proximity to the modulus maxima of the output sensitivity coefficients can be selected. A second degree of freedom is the dominance factor η_j^r in Eq. (4.10) which plays a critical role in the quality of the parameter error estimates. A third degree of freedom

is the adaptation step size $\mu_i(q)$ in Eq. (4.17) that can be adjusted at each iteration based on the level of confidence in the corresponding parameter error estimate $\widehat{\Delta\theta}_i$.

4.4.1 Proximity to Edge Points

It has been reported widely that 'edges' represent the most distinguishable aspect of images and are used extensively for data condensation [22]. Edges are detected in the time-scale domain by the modulus maxima of the CWTs [22], as indicators of the decay of the CWT amplitudes across scales. Following the definition by Mallat [22], a modulus maxima at any point (t_0, s_0) on the time-scale plane is a local maxima of $|W\{f\}(t, s_0)|$. This implies that at a modulus maxima [22]

$$\frac{\partial W\{f\}(t_0, s_0)}{\partial t} = 0 \tag{4.25}$$

where this maximum is a strict maximum and the maxima lines are the connected curves $s(t)$ in the time-scale plane along which all points are modulus maxima.

There is considerable evidence that the CWT modulus maxima capture a significant content of the image, and that signals can be reconstructed via the CWT modulus maxima [22]. This motivates giving preference to the CWT modulus maxima. To this end, only those parameter signature pixels can be selected that correspond to the largest wavelet coefficients of the associated output sensitivity. This selection strategy is illustrated in Fig. 4.4 where on the left is the full parameter signature superimposed on the modulus maxima of the wavelet coefficient of the corresponding output sensitivity, and on the right is the refined parameter signature with its pixels selected to correspond to the largest wavelet coefficients of the output sensitivity. As is illustrated by the two parameter signatures, this strategy achieves the objective of mostly selecting the pixels intersecting or of close proximity to the modulus maxima of the output sensitivity.

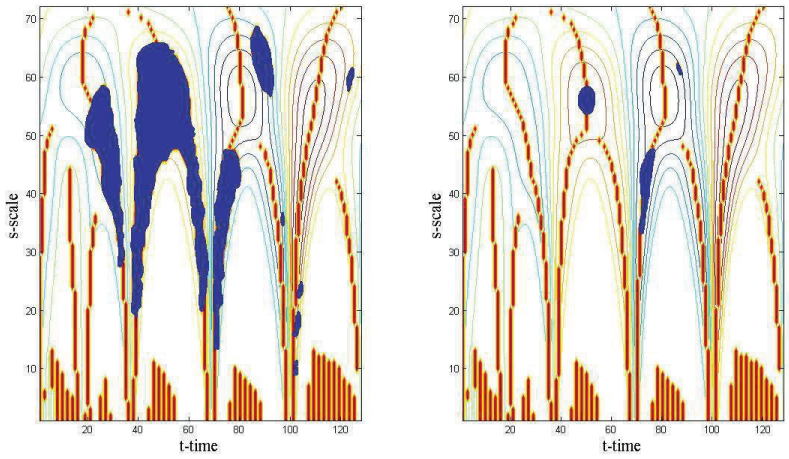

Figure 4.4. Parameter signature pixels shown together with the modulus maxima of the wavelet coefficients of the corresponding output sensitivity. The right plot is the full parameter signature, whereas the left plot shows the parameter signature reduced to 50 pixels closest to the modulus maxima of the output sensitivity.

The above strategy of refining the parameter signatures to a reduced size, not only pre-filters the signature pixels such that only those pixels containing the most essential information are used in the parameter error estimate, but also restricts and unifies the number of pixels of every parameter signature, thereby resulting in a compact and uniformly formed Jacobian, $\mathbf{\Phi_s}$, in Eq. (4.14). To underline this point, shown respectively in Fig. 4.5 are the parameter error estimates at the pixels of the parameter signatures in Fig. 4.4. Although the parameter error estimates from the refined parameter signature on the right are not uniform in sign, they are far more condensed and, therefore, of lower entropy than those on the left.

The ramification in parameter estimation of the above parameter signature refinement strategy is evaluated in application to the van der Pol oscillator, introduced below as the second platform of this paper. Parameter estimation of the van der Pol oscillator faces non-convex error surfaces and local minima, which are challenging to navigate by gradient-based parameter estimation methods such as NLS and PARSIM.

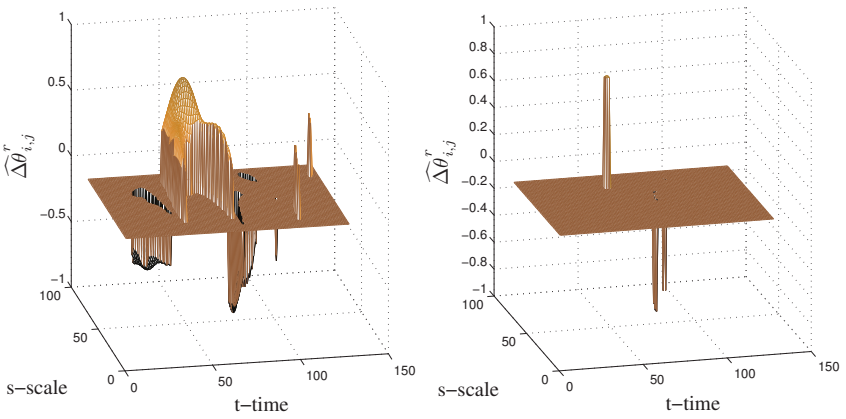

Figure 4.5. The parameter error estimates from the pixels of the parameter signatures in Fig. 4.4. The left plot shows the parameter error estimates of the original parameter signature, whereas the right plot shows the estimates at the select (fifteen) pixels.

Platform 2: The van der Pol oscillator is an example of a self-excited nonlinear oscillator, having the form [37]

$$\begin{aligned} m\ddot{x} - c(1-x^2)\dot{x} + kx &= 0 \\ \mathbf{y} &= \begin{bmatrix} x & \dot{x} \end{bmatrix}^T \end{aligned} \tag{4.26}$$

with its true parameters defined as $\boldsymbol{\Theta}^* = [m^* \;\; c^* \;\; k^*]^T = [375 \;\; 10000 \;\; 75000]^T$. As in Chua's circuit, the prediction error of this system reflects the difference between the true and nominal parameters, as $\epsilon(t) = \hat{\mathbf{y}}(t, \boldsymbol{\Theta}^*) - \hat{\mathbf{y}}(t, \bar{\boldsymbol{\Theta}})$, with the nominal parameters set as $\bar{\boldsymbol{\Theta}} = [\bar{m}, \bar{c}, \bar{k}]^T = [0.8\theta_1^*, 1.25\theta_2^*, 0.8\theta_3^*]^T = [300, 12500, 60000]^T$. The system was simulated in response to the initial condition $x(0) = 0.02,\ \dot{x}(0) = 0$ with a short time-window of 1.27 sec to avoid chaotic behavior and accommodate its first-order approximation.

The effect of parameter signature refinement on parameter estimation by PARSIM is shown in Fig. 4.6, which shows the estimates of the van der Pol oscillator parameters by the full and refined parameter signatures, respectively. The results clearly indicate the

higher accuracy achieved by the refined parameter signatures, hence giving credence to the parameter signature refinement strategy adopted.

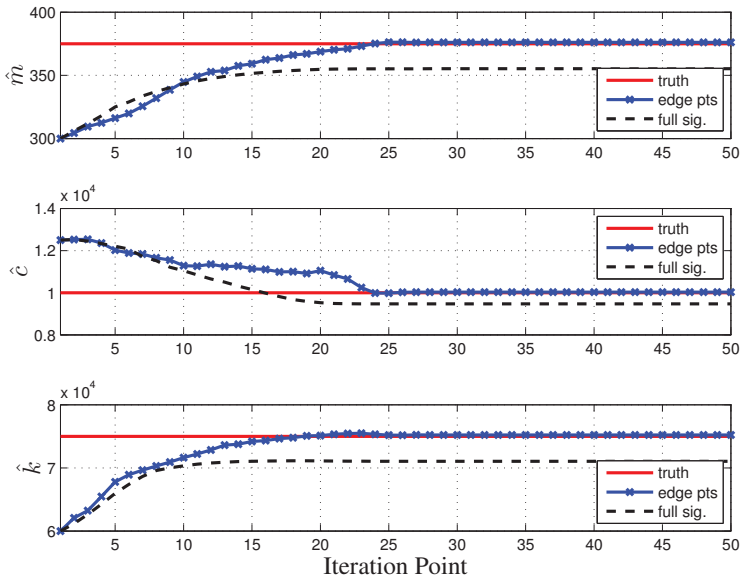

Figure 4.6. Estimates of the van der Pol oscillator parameters by the full and refined parameter signatures

4.4.2 Dominance Factor Adaptation

PARSIM relies on the dominance factors η_j^r in Eq. (4.10) to extract the parameter signatures. These parameter signatures then determine the regions of the time-scale domain to be included in PARSIM's parameter estimation solution. Therefore, the dominance factors play a critical role in affecting not only the size of the parameter signatures and their pixel locations but also the magnitude of the corresponding parameter error estimates and their entropies. This is illustrated in Fig. 4.7 for two parameter signatures obtained at different dominance factors. As a rule, a higher dominance factor results in a smaller parameter signature, as is clear from the smaller parameter signature extracted by a higher dominance factor on the right. Smaller parameter signatures also tend to yield lower entropies for their

corresponding parameter signatures, as indicated by the smaller entropy of the parameter error estimates on the right of Fig. 4.7. Therefore, it appears that a suitable strategy for dominance factor selection should favor higher dominance factors. However, too high a dominance factor can lead to a null parameter signature. It is, therefore, essential to the operation of PARSIM to have a strategy whereby a suitable dominance factor is continually selected such that the highest overall quality parameter signatures are extracted for each CWT of an output at each iteration of parameter estimation.

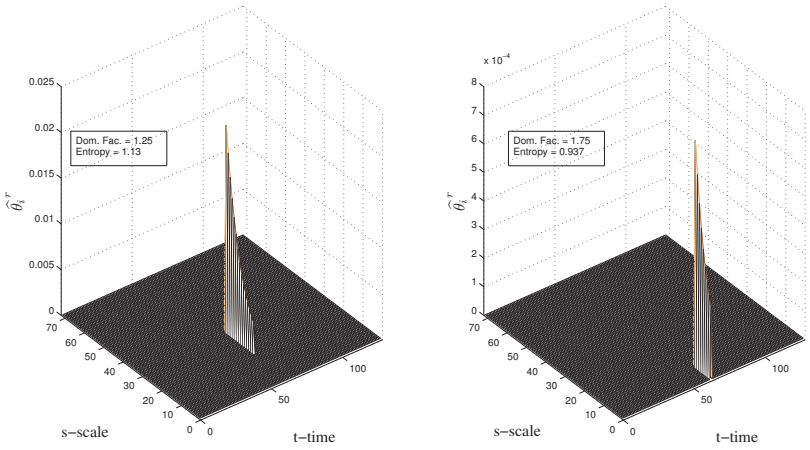

Figure 4.7. Sample effect of the dominance factor on the size of the parameter signature and its parameter error estimates

The strategy adopted for selection of each dominance factor η_j^r extracts parameter signatures at a pre-specified set of dominance factors and then selects the dominance factor yielding parameter error estimates with the least overall entropy. This selection strategy has the form

$$\eta_j^{r*} = \arg\min_{\eta_j^r} \sqrt{\sum_{i=1}^{Q} \left(S_{i,j}^r(\eta_j^r, \widehat{\Delta\theta}_{i,j}^r) \right)^2} \tag{4.27}$$

where η_j^{r*} denotes the selected dominance factor for the rth CWT of the jth output yielding the least L^2 entropy norm of the parameter error estimates among the dominance factors considered. Another benefit of the devised dominance factor selection strategy is

its assurance of maximal parameter signature extraction by avoidance of null parameter signatures that are represented by infinite entropy values. Null parameter signatures, as shown in Table 4.1, not only hinder the "least-squares solution" of PARSIM but also lead to zero parameter error estimates (Table 4.2) that denigrate the effectiveness of its "separate parameter estimate solution."

For illustration purposes, shown in Fig. 4.8 are the selected dominance factors for three different CWT/output combinations of the van der Pol oscillator at different iteration points of parameter estimation. From the dynamics of the selection process it is clear that different dominance factor levels are selected for each CWT/output combination among the five choices available. For instance, the dominance factor selected in the left plot is mostly at the lower end, whereas the ones in the middle and right plots are gravitating toward the higher end.

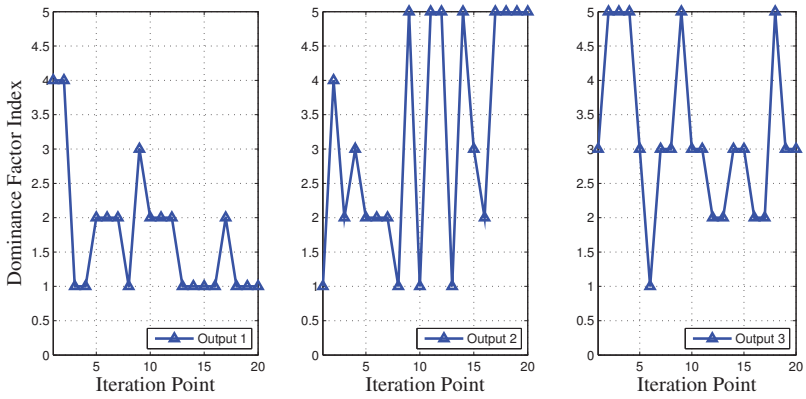

Figure 4.8. Illustration of dominance factor selection during estimation of the van der Pol oscillator parameters

The ultimate test of the adopted selection strategy, however, lies on its improvement of parameter estimation by PARSIM. One measure of parameter estimation quality is the condition number of the Jacobian $\mathbf{\Phi_s}$ (Eq. (4.14)), which is examined for the selected dominance factor of the van der Pol oscillator in Fig. 4.9 among the condition numbers of the Jacobian matrices of the dominance factors considered. The results clearly indi-

cate the effectiveness of the devised dominance factor selection strategy in yielding the best-conditioned Jacobian matrix for parameter estimation, even though the selection is performed independent of the condition number.

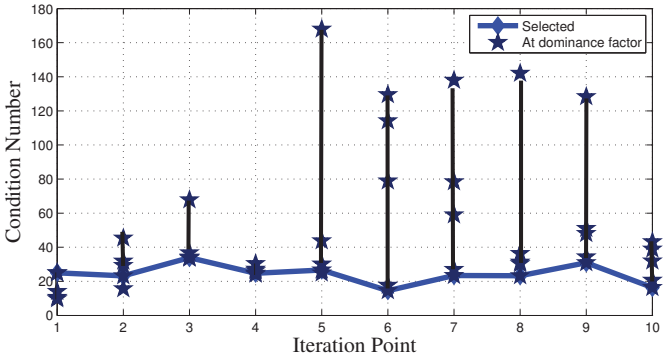

Figure 4.9. The condition number of Φ_s changes with dominance factor.

Next examined is the effectiveness of the adopted dominance factor selection strategy on parameter estimation. For this, the effect of the selection strategy is evaluated in estimation of the van der Pol oscillator parameters. Shown in Fig. 4.10 are the prediction and precision errors of the van der Pol oscillator parameter estimates at different iteration points (q in Eq. (4.17)) obtained with dominance factor adaptation (noted as variable DF). Shown in Fig. 4.10 are also the errors from two other estimation runs at two fixed dominance factors. The prediction error in Fig. 4.10 represents the error between the true and modeled outputs, as $\sum_k |\epsilon(t_k)|$, and the precision error, ϵ_θ, represents the squared sum of the parameters error at each iteration q, formulated as

$$\epsilon_\theta(q) = \sum_{i=1}^{Q} \left(\frac{\theta_i^* - \hat{\theta}_i(q)}{\hat{\theta}_i(q)} \right)^2 \tag{4.28}$$

to denote the accuracy of the estimated parameters. It is noted that in practice the true parameter values θ_i^* are not known to allow estimation of the precision error. However, in simulation based studies such as this they provide an effective means of evaluating

the validity of parameter estimates, beyond the prediction error minimization capacity of the method. Both the prediction and precision errors in Fig. 4.10 show the effectiveness of the devised dominance factor adaptation strategy in improving parameter estimation as compared to using a fixed dominance factor throughout the parameter estimation run. The above results, therefore, show that the adopted dominance factor selection strategy not only leads to a Jacobian that has the best condition number, among the choices considered, but also improves the accuracy of parameter estimation.

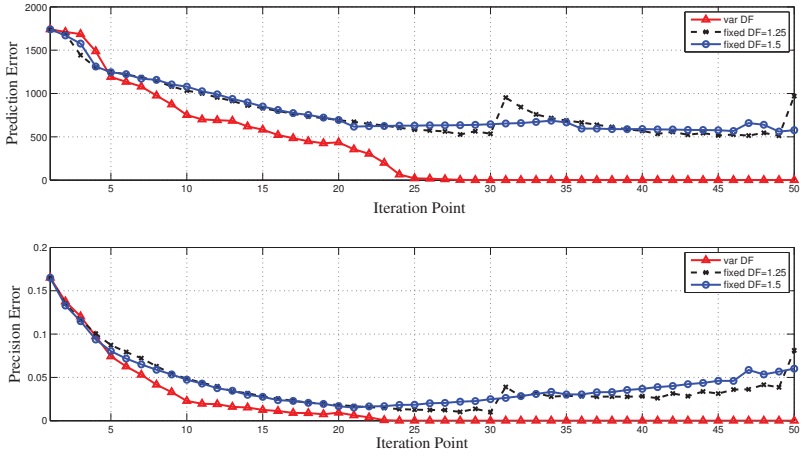

Figure 4.10. Illustration of how optimal dominance factor effects convergence

4.4.3 Weight Assignment

The quality measure of each estimate $\widehat{\Delta\theta}^r_{i,j}$ in PARSIM is its Shannon entropy. Therefore, in the separate parameter estimate solution, the weights $w^r_{i,j}$ in Eq. (4.20) are assigned such that higher weights are assigned to parameter estimates of lower entropy. Accordingly, the weights are defined as

$$w^r_{.,j} = \max(S^r_{.,j}) - S^r_{.,j} \tag{4.29}$$

where $\max(S^r_{.,j})$ denotes the maximum entropy of all the parameter error estimates at the current iteration. The above weight assignment strategy, which is consistent with

associating lower entropies with higher quality estimates, will assign the highest weight to the parameter error estimate with the lowest entropy.

4.4.4 Step Size Adaptation

The magnitude of the adaptation step size $\mu_i(q) \in (0, 1]$ in Eq. (4.17) represents the confidence in the parameter error estimate $\widehat{\Delta\theta}_i(q)$. Using lower values of μ_i tend to render more stable estimation runs, but they prolong estimation. In time-based estimation methods, like NLS, the magnitude of μ is the same for all parameters (Eq. (4.4)) and is usually selected according to the convexity of the error surface. In PARSIM, however, the $\mu_i(q)$ in Eq. (4.17) can be selected separately for each parameter at each iteration according to the quality of the parameter error estimate at that iteration. The requisite for adapting the $\mu_i(q)$ is the ability to assess the confidence in $\widehat{\Delta\theta}_i(q)$, which is determined by PARSIM according to the quality of its constituents, $\widehat{\Delta\theta}^r_{i,j}$.

As was discussed before, the quality measure of each estimate $\widehat{\Delta\theta}^r_{i,j}$ in PARSIM is its Shannon entropy. However, the assignment of $\mu_i(q)$ requires the further step of assigning confidence to the $\widehat{\Delta\theta}_i(q)$ based on the quality measures of its constituents $\widehat{\Delta\theta}^r_{i,j}(q)$. Our studies indicate that the adaptation of $\mu_i(q)$ is better achieved according to the variance of the estimates, $\gamma^r_{i,j}$ in Eq. (4.23), and their unidirectionality $d^r_{i,j}$ in Eq. (4.24). The adaptation of $\mu_i(q)$ is performed within a nominal range $\bar{\mu} = [\bar{\mu}_{min}, \bar{\mu}_{max}]$, which is specified according to the overall convexity of the error surface. The value of $\mu_i(q)$ at each iteration is formulated as

$$\mu_i(q) = (1 - \bar{\mu}_{max}) * \xi_i(q) + (\bar{\mu}_{max} * \phi_i(q)) \tag{4.30}$$

where ξ_i is a factor to account for the variance of the parameter error estimates, $\gamma^r_{i,j}$, and ϕ_i is the factor associated with their unidirectionality. According to the formulation in Eq. (4.30), higher values of ξ_i and ϕ_i would lead to an adaptation step size μ_i closer to the upper limit, $\bar{\mu}_{max}$. The computation of these factors is discussed below.

- *Variance factor* ξ_i: The function of ξ_i is to boost μ_i when the individual parameter estimates $\Delta\theta_{i,j}^r$ associated with parameter θ_i have a small variance. For its computation, the largest weight among the $w_{i,j}^r$ in Eq. (4.20) is used as a reference. The index of this largest weight is defined as

$$I_i = (i, j*, r*) \quad \ni \quad w_{I_i} = max(w_{i,j}^r) \;\; \forall j = 1, \ldots, R; \;\; r = 1, \ldots, P \tag{4.31}$$

where I_i denotes the index of the $\Gamma_{I_i,j}^r$ (or $\widehat{\Delta\theta}_{I_i,j}^r$) associated with the maximum weight (minimum entropy) among the $\Gamma_{i,j}^r$ of the ith parameter, $\widehat{\Delta\theta}_i$. The variance γ_{I_i} of the parameter error estimates $\widehat{\Delta\theta}_{I_i,j}^r$ estimated by Eq. (4.23) is then normalized as

$$\psi_i = |\ln(\gamma_{I_i})| \tag{4.32}$$

where ln denotes natural logarithm. Since $\gamma_{I_i} < 1$, the above normalization provides an inverse mapping of smaller variances to larger ψ_i. The range of ψ_i is then mapped by interpolation to the range of the nominal adaptation step size $\bar{\mu}$ by an interpolation line having the slope α and intercept β. The variance factor ξ_i is then computed as

$$\xi_i = \alpha * \psi_i + \beta \tag{4.33}$$

- *Directionality factor* ϕ_i*:* The computation of the directionality factor is considerably more straightforward. It is defined to simply represent the average unidirectionality of the parameter error estimates $\widehat{\Delta\theta}_{i,j}^r$, as

$$\phi_i = \frac{1}{RP} \sum_{j,r}^{R,P} |d_{i,j}^r| \tag{4.34}$$

For illustration purposes, the estimates of the van der Pol oscillator parameters obtained with variable μ_i are shown in Fig. 4.11 along with estimates obtained using different fixed μ_i. The results clearly indicate the effectiveness of the adaptation mechanism devised for μ_i.

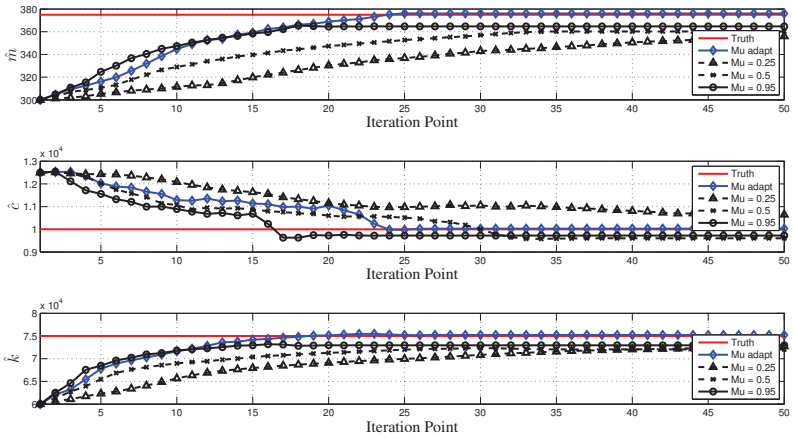

Figure 4.11. Parameter estimates of the van der Pol oscillator obtained with a variable step size as well with several fixed step sizes

4.5 Performance Evaluation

The contribution of PARSIM is to allow incorporation of shape attributes in parameter estimation. It achieves this by including selected portions of output sensitivities and prediction error wavelet coefficients in parameter estimation, to allow managing the enormousness of data generated by various CWTs of the model outputs. There are two aspects of PARSIM's performance. One aspect concerns the internal workings of PARSIM, as it pertains to its different solutions (i.e., least-squares versus separate parameter estimates) and different CWT combinations. The other aspect concerns the potential advantages of PARSIM in comparison to time-based parameter estimation.

The performance of gradient-based parameter estimation methods is dependent upon the global convexity of the error surface, therefore, the general performance of PARSIM cannot be comprehensively evaluated independent of its application platform. In lieu of such generalization capacity, we have sufficed to presenting results from both its solutions and with different CWTs, to provide a qualitative view of their influence on parameter estimation cases considered.

Although PARSIM benefits from several degrees of freedom that are unavailable to time-based parameter estimation, its ultimate advantage is realized when the shape attributes provide a competitive advantage to the magnitude of output sensitivities and prediction error. Again, in the absence of a generalized framework, results are provided to illustrate behavioral aspects that can be gained by the inclusion of shape attributes. The results presented here are, therefore, meant to only highlight those aspects of PARSIM's performance that seem to offer an advantage over magnitude-based parameter estimation. In that light, we have presented the results of PARSIM together with that of NLS, solely to provide a basis for evaluating its performance and not as evidence of its overall superiority to time-based parameter estimation.

4.5.1 The Two PARSIM Solutions

The two solutions of PARSIM are formulated in Eqs. (4.13) and (4.19), respectively. The fundamental difference between the two solutions is the use of the covariance matrix ($\mathbf{\Phi_s}^T\mathbf{\Phi_s}$) in the least-squares (LS) solution (Eq. (4.13)), which incorporates the cross-correlation between the output sensitivities (i.e., the off-diagonal components of the covariance matrix) in estimation of the parameter errors, $\Delta\theta_i$. In this light, the separate parameter estimate solution in Eq. (4.19) can be viewed as associated solely with the diagonal elements of the covariance matrix. To provide a comparison between the two solutions, hence the significance of the off-diagonal elements of the covariance matrix, the parameters of both the Chua's Circuit and the van der Pol oscillator were estimated by each of

these solutions. The prediction and precision errors of the estimates during the estimation run are shown in Fig. 4.12. The results from the van der Pol oscillator indicate that the separate parameter estimate solution becomes entrapped in a local minima, even though the prediction error reaches zero. Those from the Chua's circuit indicate that the LS solution provides a much smoother convergence profile, although both solutions converge to the correct parameter values. Overall, the results in Fig. 4.12 clearly indicate the more effective performance of the LS solution. Therefore, the LS solution is designated as the solution of choice by PARSIM, unless the Jacobian Φ_s becomes rank deficient due to the absence of signatures for a parameter by any of the CWT/output combinations (e.g., see Table 4.1). In such case and for that iteration, the separate parameter estimate solution is used as the backup solution.

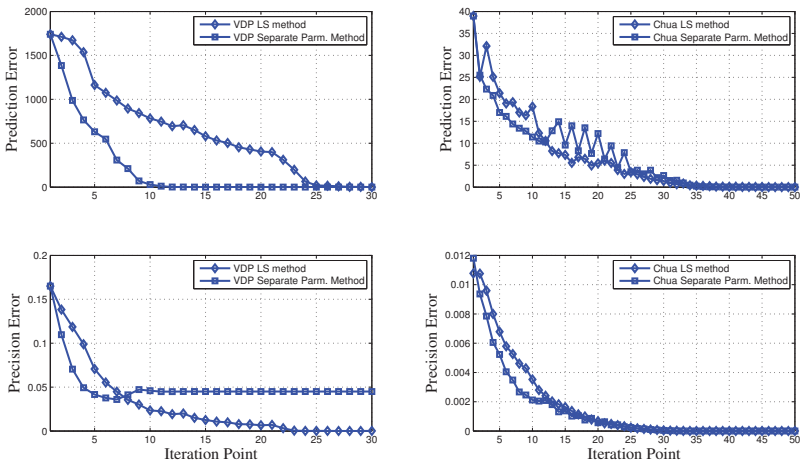

Figure 4.12. Prediction and precision errors of parameter estimates of the van der Pol oscillator (left) and Chua's circuit (right) by each of the two PARSIM solutions

4.5.2 Combination of Shape Attributes

The salient feature of PARSIM is its incorporation of shape attributes in parameter estimation. Therefore, its effectiveness vis-á-vis time-based (magnitude-based) parameter

estimation is contingent upon the added information content provided by the shape attributes over and beyond the magnitude. As demonstrated later, one condition of such contingency, that we have identified so far, is the smoothness of output sensitivities. Yet, given smooth output sensitivities and the preference for the shape attributes, the question still remains as which shape attributes to consider. To illustrate the significance of shape attributes in parameter estimation, shown in Fig. 4.13 are the parameter estimates of the van der Pol oscillator and Chua's circuit by different transform combinations. Even though the results are case-specific, the precision errors on the left illustrate that only one combination of the CWTs; i.e., Gaussian smoothing together with the Gauss and Sombrero CWTs, is effective in finding the global minimum for the van der Pol oscillator. On the other hand, the precision errors on the right indicate the parameter estimates of the Chua's circuit are more forgiving in that of the six transform combinations, only two fail to provide adequate information content and four of them lead the estimates to their true values. It is interesting to note that unlike the corresponding precision errors, the prediction errors on the left all reach zero, underlining the presence of local minima for the van der Pol oscillator. Another point of interest in Fig. 4.13 is the observation that the best estimation results correspond to the largest combination of transforms. Even though anecdotal and not of value in and of itself, this observation highlights PARSIM's effective integration capacity that enables it to benefit from the added information of various transforms for improved parameter estimation.

4.5.3 Convergence Characteristics

Defining the convergence characteristics of PARSIM is not an easy task, because of the case-specificity of the parameter estimation problem. Furthermore, our experience with PARSIM is limited to a few platform applications, corresponding to a limited range of error surface characteristics. Therefore, the results presented are not meant to provide a definitive and comprehensive view of PARSIM's performance, they are to rather demonstrate only

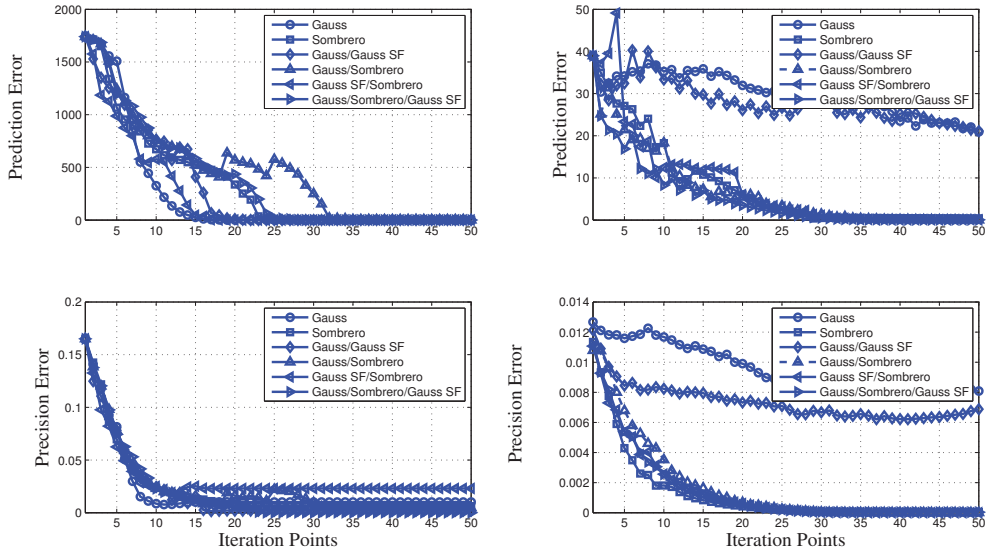

Figure 4.13. Parameter estimates of the van der Pol oscillator (left) and Chua's circuit (right) obtained with different transform combinations

aspects of PARSIM that are noteworthy as a parameter estimation solution. One such aspect is the potential for faster convergence. Another aspect is PARSIM's tendency to be less vulnerable to local minima entrapment. Yet another aspect of PARSIM is its sensitivity to the smoothness of output sensitivities. The results provided next illustrate these aspects of PARSIM.

4.5.3.1 Speed of convergence

In general, PARSIM is a computationally intensive method, due to the added computation associated with wavelet transformation, signature extraction and the selection of its various degrees of freedom. As such, any potentially faster convergence rates attained by PARSIM would be overshadowed by its longer computation times, except in cases where simulation times dominate the times used for parameter estimation. While Chua's circuit does not represent such a case, it can be used to evaluate the speed of convergence of PARSIM. To this end, fifty estimation runs of Chua's circuit's parameters were performed

by PARSIM and NLS with random initial parameter values within 2% of the nominal parameter values $\bar{\boldsymbol{\Theta}} = [0.95\,\theta_1^*,\ 1.05\,\theta_2^*,\ 0.95\,\theta_3^*,\ 1.05\,\theta_4^*,\ 0.95\,\theta_5^*]$. Shown in Fig. 4.14 are the prediction and precision errors of these estimation runs. They indicate faster convergence rates achieved by PARSIM than NLS. However, these results are not to be generalized as a characteristic of PARSIM, as we expect numerous scenarios to exist wherein PARSIM's performance would be inferior to magnitude-based parameter estimation.

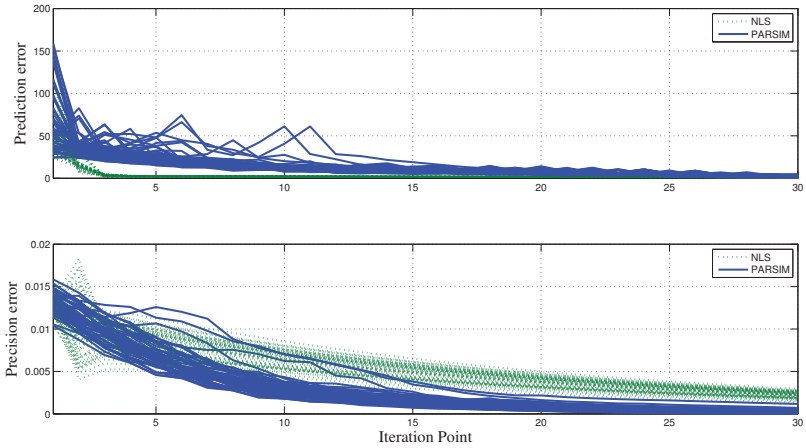

Figure 4.14. Prediction and precision errors of fifty estimation runs of Chua's circuit parameters obtained by PARSIM or NLS with different initial parameter values

4.5.3.2 Evasion of local minima

A potential hazard of gradient-based parameter estimation is entrapment in local minima with non-convex error surfaces. In these cases, the prediction error could reach a minimum of zero but not the precision error. A case in point is the van der Pol oscillator, as represented by the results in Fig. 4.13. To facilitate visualization, the error surface of the van der Pol oscillator is plotted in Fig. 4.15 in terms of only two of its parameters, c and k. Also shown in Fig. 4.15 are the trajectories of parameter estimates by both PARSIM and NLS from two starting points on the non-convex regions of the error surface. The results clearly indicate the marked difference between the two trajectories. The NLS solutions

end in local minima, whereas the solutions from PARSIM converge to the global minimum (bottom of the convex region). However, the results in Fig. 4.15 could be due to the initial conditions used, or may be specific to the application platform. To provide a slightly more diversified study of this aspect of PARSIM, a third platform is described below which also poses the local minima challenge.

Platform 3: The parameter estimates of the nonlinear mass-spring-damper (MSD) model

$$m\ddot{x} + c\dot{x}|\dot{x}| + kx^3 = 0 \tag{4.35}$$

can also be entrapped in local minima when the output represents the free response of the displacement x to initial conditions. In this model, m denotes the system mass, c is its damping coefficient, and k is its spring constant. The true model parameter values were set as $\boldsymbol{\Theta}^* = [m^*, c^*, k^*] = [375, 9800, 130000]$ and the nominal parameter values as $\bar{\boldsymbol{\Theta}} = [0.8\,\theta_1^*, 1.25\,\theta_2^*, 0.8\,\theta_3^*]$. The output comprised the free response of the MSD to the initial conditions $x(0) = 0.2$ and $\dot{x}(0) = 0$.

The capacity of PARSIM in evading local minima was tested in application to both the van der Pol oscillator and the MSD. For this purpose, fifty estimation runs of the van der Pol oscillator and MSD parameters were performed with random initial values by both PARSIM and NLS. The random initial values for the van der Pol oscillator were within $\pm 10\%$ of the nominal parameter values $\bar{\boldsymbol{\Theta}} = [0.8\,\theta_1^*,\ 1.25\,\theta_2^*,\ 0.8\,\theta_3^*]$ and those of the MSD were within $\pm 1\%$ of the nominal parameter values $\bar{\boldsymbol{\Theta}} = [0.8\,\theta_1^*,\ 1.25\,\theta_2^*,\ 0.8\,\theta_3^*]$. The prediction and precision errors of the estimation runs are shown in Fig. 4.16, where the left plots are associated with the van der Pol oscillator and the right plots with the MSD. The prediction errors in the top plots indicate the success of NLS in zeroing the prediction error far more rapidly than PARSIM, albeit at erroneous parameter values, as indicated by the generally non-zero values of the precision error by NLS in the bottom plots. PARSIM,

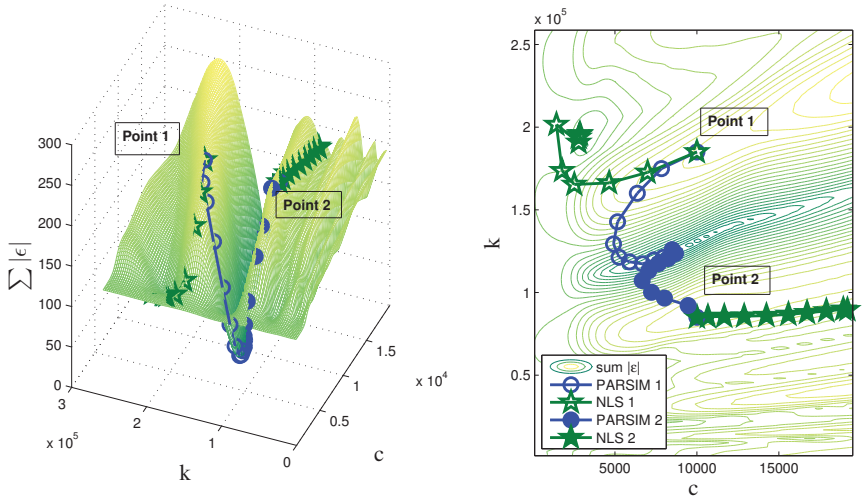

Figure 4.15. Two cases where PARSIM finds the global minimum when NLS gets entrapped in a local minima

on the other hand, takes considerable more iterations to minimize the prediction error, but it is far more successful at reaching the correct parameter values, as represented by the generally smaller values of the precision errors obtained by PARSIM in the bottom plots. We attribute the better precision of PARSIM to its separate nature of estimation of the model parameters.

4.5.3.3 Smoothness of output sensitivities

PARSIM relies on the shape attributes of output sensitivities, therefore, its performance depends on successful characterization of these shape attributes. By the same analogy, superfluous spikes in the output sensitivities that are caused by idiosyncrasies of numerical simulation would adversely distort the parameter signatures and hamper parameter estimation. This aspect of PARSIM is illustrated in the context of the van der Pol oscillator. Shown in the top plots of Fig. 4.17 are the unfiltered (left) and smoothed (right) output, x, of the van der Pol oscillator together with the output sensitivities, in the middle plots, obtained before and after smoothing of this output. The ramification of the smoothing on

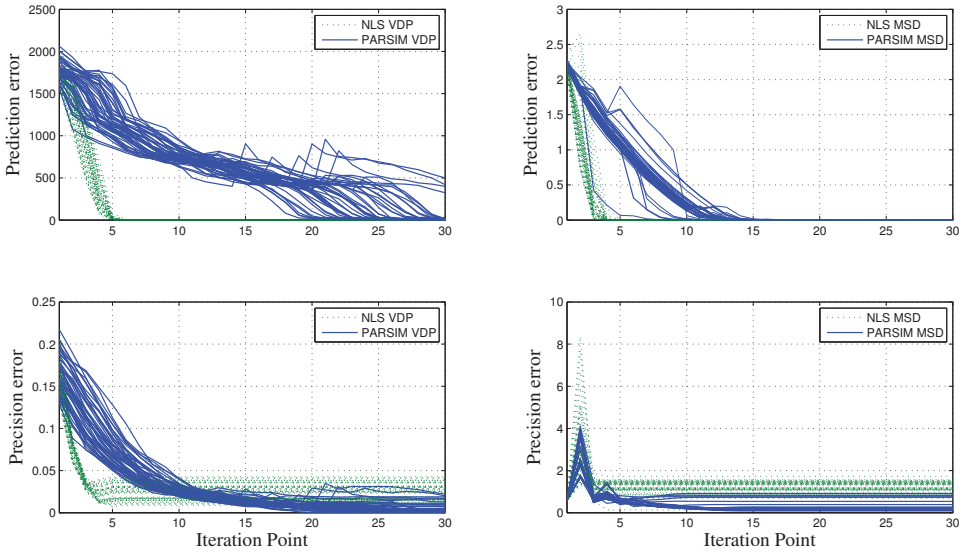

Figure 4.16. Prediction and precision errors of fifty estimation runs of the van der Pol oscillator parameters (left) and MSD parameters (right) obtained with random initial parameter values

the parameter signatures is shown via the parameter signature of c in the bottom plots of Fig. 4.17. Of note are the non-analytic spikes in the output sensitivities on the left, which have been smoothed by filtering the output on the right. A significant ramification of such smoothing is seen in the parameter signature of parameter c obtained by Gauss CWT, in the bottom plots of Fig. 4.17. This parameter signature indicates the regions of the time-scale plane wherein the slope of $\partial x/\partial c$ exceeds the slopes of the other output sensitivities, $\partial x/\partial m$ and $\partial x/\partial k$, by the dominance factor $\eta = 1.5$. According to the parameter signature extracted from the unfiltered output, these regions correspond to approximately 2.6 seconds and 3.75 seconds. However, the region in the parameter signature extracted from the smoothed output (bottom right) only corresponds to 2.6 seconds, thus excluding the region at 3.75 seconds. Noting that the parameter error estimates associated with the 3.75-second region are in the opposite direction to the estimates at 2.6 seconds, the exclusion of this second region improves the uniformity of the parameter error estimates.

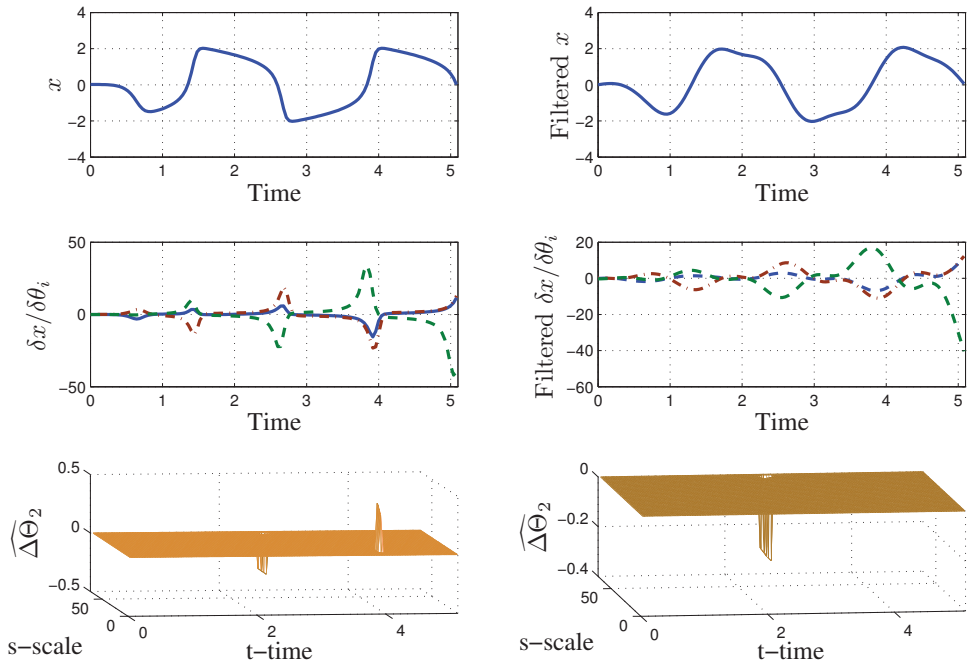

Figure 4.17. Unfiltered and smoothed (low-pass filtered) output sensitivities of the van der Pol oscillator (middle plots) obtained, respectively, from the unfiltered and smoothed output (top plots). Also shown in the bottom plots are the parameter signatures of c from the unfiltered and filtered output sensitivities by the Gauss WT.

Any potential improvement of the parameter signature quality by smoothing should be represented in the entropy of parameter signatures as well. For evaluation purposes, listed in Table 4.3 are the entropy values of six parameter signatures of parameter c by Gaussian smoothing and Gauss and Sombrero CWTs of the van der Pol oscillator outputs. The entropy values are lower for four of the parameter signatures from smoothed outputs, indicating an enhanced overall information content as the result of smoothing. A direct ramification of this enhanced information content, if true for all parameters and at various instances of parameter estimation, ought to improve the performance of PARSIM. To evaluate this assertion, several estimation runs with different initial parameter values of the van der Pol oscillator parameters were obtained with and without smoothing its outputs.

The prediction and precision errors of the estimates, shown in Fig. 4.18, indicate a faster convergence of the prediction error due to smoothing, albeit not at a higher precision. The improved speed of convergence of PARSIM in Fig. 4.18 due to smoothing gives credence to PARSIM's predisposition to smooth shapes.

Table 4.3. Entropy values of the parameter signatures obtained for parameter c of the van der Pol oscillator from Gaussian smoothing and Gauss and Sombrero CWTs of its outputs

	Parameter Signature Entropies					
	CWT_1^1	CWT_1^2	CWT_1^3	CWT_2^1	CWT_2^2	CWT_2^3
unFiltered	1.236	1.236	1.061	1.175	1.028	1.184
Filtered	1.231	1.035	0.937	0.908	1.115	1.252

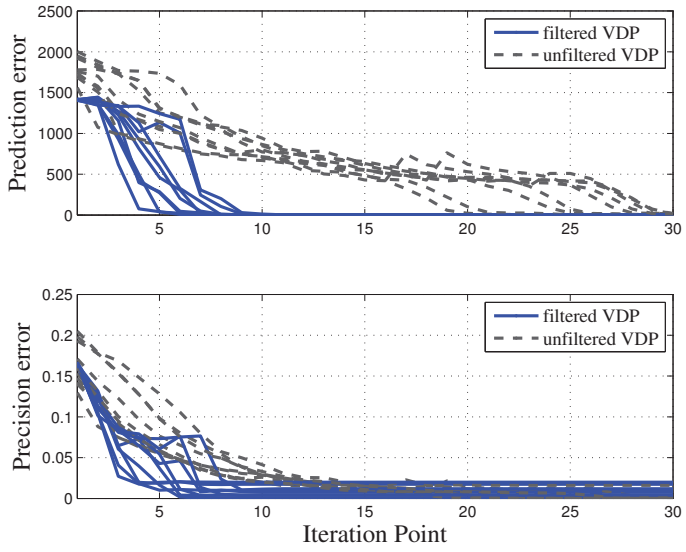

Figure 4.18. Unfiltered and filtered parameter estimation of the van der Pol oscillator circuit

4.6 Application to Gas-Turbine Parameter Estimation

There are classes of simulations in which despite smoothing the data to remove fictitious features, i.e., spikes, as well as utilizing all of PARSIM's transparencies and degrees of freedom, the parameters fail to converge. The estimation of the level of performance degradation of gas-turbine engine is an example of such a case. The model used in this study is the same generic engine model used in the direct method for health parameter estimation described in the first part of this thesis. The inverse method is used to quantify the level of damage of the same ten parameters comprising of the efficiency and flow capacity of the five major components: low pressure compressor(LPC), high pressure compressor (HPC), high pressure turbine (HPT), low pressure turbine (LPT), and fan. Attempting to estimate the ten parameters without filtering, results in the lack luster performance shown in Fig. 4.19 where it can be plainly seen that nearly half of the parameters fail to close to their respective targets. It should be noted that with exception to the LPT_{FC} health parameter, NLS does not appear to have much difficultly converging to the estimation and is shown on the plot as a reference.

Fig. 4.20 is the analog of Fig 4.17. The top plots depict the unfiltered (left) and filtered (right) time trace of the output of the pressure measurement at station 2.5 ($P_{2.5}$) located between the low and high pressure compressor. The middle plots are the output sensitivities of $P_{2.5}$ w.r.t. LPC_{eff} along with the output sensitivities of three other parameters which have been added as reference. Of note are the non-analytic spikes at approximately twelve and twenty-eight seconds in the unfiltered plot in the middle left plot. These spikes are the result of numerical anomalies rather representative of any true physical phenomena. Also of note are the output sensitivities of the other three parameters which show the relative flatness in the data. The flatness of the data is the other issue preventing successful estimation of the parameters in this particular simulation. Data devoid of unique and distinguishing features inhibit the necessary condition of dominance at pixel locations

between parameters and requires relatively low dominance factors, in this case 1.10, to extract any parameter signatures. Finally the lower plots are the parameter signatures of $\partial P_{2.5}/\partial LPC_{eff}$ produced using the Gauss CWT. The parameter error coefficients are at the locations where they dominate all the other parameter error coefficients produced by the same Gauss CWT and dominance factor at that location on the time-scale plane. These parameter signatures resulting from low dominance factors tend to be of low quality as can be seen in the lower left hand plot of Fig. 4.20 exhibiting bi-directional coefficients as in the case of the van der Pol oscillator indicating dubious quality.

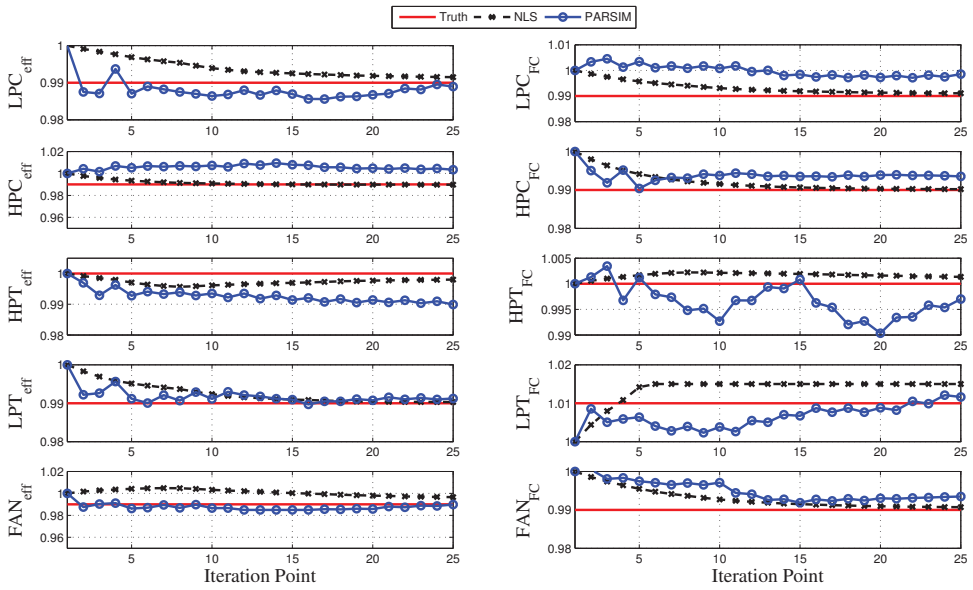

Figure 4.19. Comparison of parameter estimations of the Gas-turbine simulation using NLS and PARSIM

Filtering the data removes the spikes and results in a uni-directional parameter signature depicted in the lower right side plot of Fig. 4.20. Of note is that the dominance factor selected increased from 1.10 to 1.15. However, unlike the case of the van der Pol oscillator, the amount of information contained in the signal is not improved as measured by the entropy values. Listed in Table 4.4 are the entropy values of the coefficients associated with the parameter error updates of the seven outputs of the gas-turbine w.r.t. LPC_{eff}

transformed using the Gauss CWT. It is readily seen that there is no significant difference between the unfiltered and filtered entropies indicating that no further information could be recouped.

Table 4.4. Parameter signature entropy for the gas-turbine simulation

Filtered/unFiltered	**Parameter Signature Entropies**						
	CWT_1^1	CWT_2^1	CWT_3^1	CWT_4^1	CWT_5^1	CWT_6^1	CWT_7^1
Filtered	1.174	1.171	1.1756	1.172	1.175	1.173	1.148
unFiltered	1.176	1.157	1.175	1.173	0.825	1.174	0

Filtering the data did not have the desired impact on the convergence of the parameter estimation in that there is still not enough content contained in the parameter error updates to provide total convergence. Five test cases were conceived to test the effects of pre-filtering the data prior to calculating parameter signatures. Fig. 4.21 shows the performance comparison between the unfiltered and filtered data. Of note is the fair degree of oscillation in the unfiltered data. The filtered data, as expected, has better performance however, there is still a fair degree of error even after 25 iterations.

At this point, a discussion is in order to attempt to explain what is happening. Because PARSIM is a shape based method, in order to extract parameter signatures, the output sensitivities needs to be rich in unique and distinguishing features. Featureless output sensitivities requires low dominance factors which in turn translates into parameter signatures which do not satisfy the condition of dominance of Eq. 4.10. The major dilemma resulting from featureless output sensitivities are parameter signatures containing less than the maximum number of possible pixels or an inordinate amount of null signatures producing zero value entropies. The former will artificially deflate the value of the entropy and can reak havoc on the calculation of $w_{i,j}^r$ of the separate parameter estimation method by assigning more weight to a parameter signature that is potentially inferior to the others while the later has the effect of driving down the L^2 norm of the column [Eq. 4.27]. This in turn will

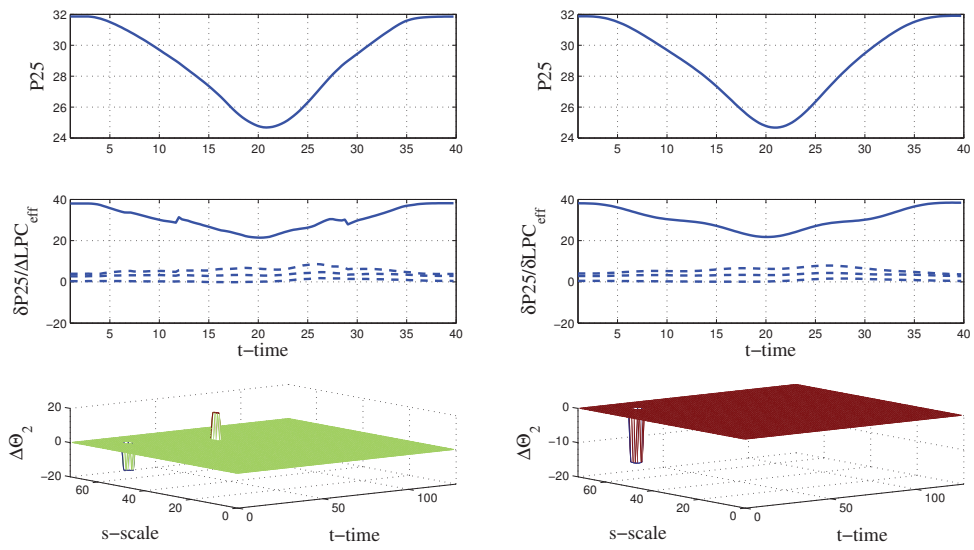

Figure 4.20. Comparison of filtered and unfiltered output sensitivities

cause the dominance factor selection process to choose an incorrect dominance factor for this output which has a grave effect on the parameter error estimate. In the example of the gas-turbine simulation, this condition caused selection of dominance factors in which outputs were void of parameter signatures for several parameters or parameter signatures located at corners of the time-scale domain. This in turn results in nonconvergence of up to 50 percent of the parameters and often lead to unrecoverable failures of the simulation.

4.7 Discussion: Inverse Method

PARSIM is a method of parameter estimation for dynamic systems that relies on the shape attributes of system outputs. The shape attributes are represented by continuous wavelet transformation of the outputs into the time-scale domain, but the surfaces that characterize the shape attributes present too vast a data content to be readily utilized in nonlinear least squares. PARSIM overcomes this impediment by considering a selected

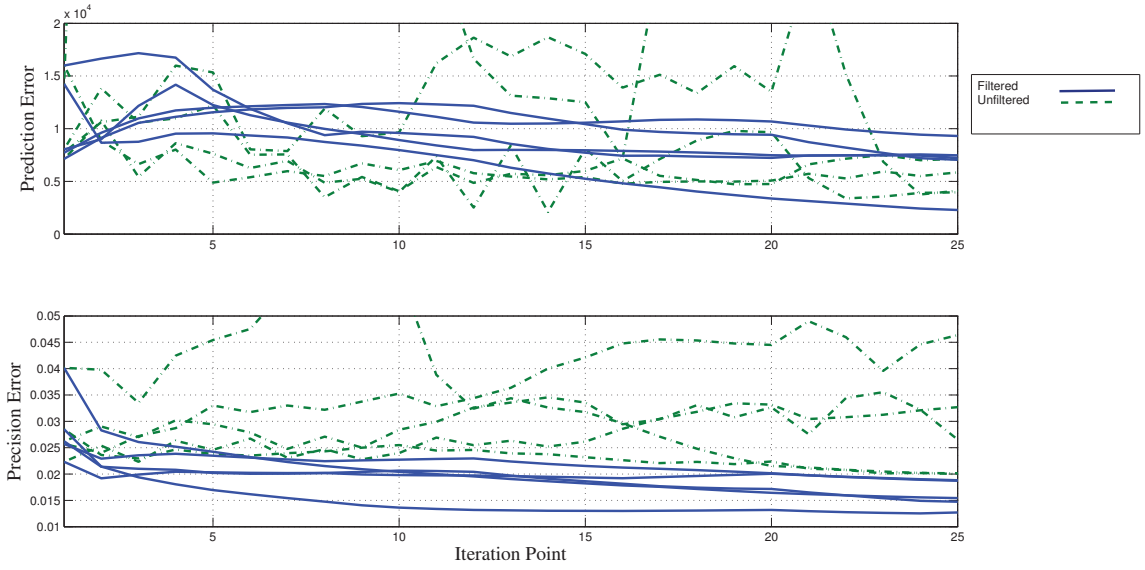

Figure 4.21. Gas-turbine simulation parameter estimation with and without filtering

subset of data points located in isolated regions of the time-scale domain and close to the modulus maxima of the corresponding wavelet coefficient surfaces.

Two different solutions are devised for parameter estimation. The first and preferred solution uses the least-square formulation. The second solution, used as recourse, is only relied upon when parameter signatures cannot be extracted for a model parameter from any of the wavelet transforms of the outputs.

Another feature of PARSIM is its capacity to use several measures of parameter signature quality as the basis for adjusting its degrees of freedom. This enables PARSIM to select the best dominance factor among a set of dominance factors considered as well as to adjust the adaptation step size associated with each parameter.

The preliminary results presented in this research validate the robustness of PARSIM's solutions and highlight some advantages of including the shape attributes in lieu of the magnitudes of the time series involved (i.e., output sensitivities and prediction errors) in cases where the level of shape variation between output sensitivities is great. Also

presented are results to indicate the benefit of the smoothness of the output sensitivities and PARSIM's potential vulnerability to superfluous spikes caused by numerical simulation. The application of PARSIM, however, is not without a cost. Its additional degrees of freedom make it more onerous to implement and its longer computation time prolongs the parameter estimation effort. As such, PARSIM should be considered when its potentially improved precision outweighs its cost of implementation.

- *Computation time*: The added computational cost of PARSIM, compared to a time-based method like NLS, is associated with (1) transformation of the involved time series (output sensitivities and prediction errors) to the time-scale domain via various CWTs, (2) extraction of the parameter signatures, (3) selection of the dominance factors, (4) computation of the adaptation step sizes, and (5) estimation of the parameter errors. In application to both Chua's Circuit and the van der Pol oscillator, 50 iterations of PARSIM on a current state-of-the-art personal computer would require 20-30 minutes depending on the number of CWTs and dominance factors considered. In comparison, the application of NLS to the same platforms would require approximately 15 seconds. Running an estimation of the Chua's circuit with a single dominance factor, for instance, requires approximately 3 seconds per iteration. The addition of a second dominance factor would double the time to 6 seconds. Therefore, the bulk of PARSIM's computation time is attributed to wavelet transformation and extracting the parameter signatures at the various dominance factors. This added computation time will be a detractor of PARSIM in applications involving quick simulation run-times. However, in applications with long simulation run-times, the time required to generate parameter signatures becomes less of a concern. In these cases, the bulk of the run-time is shifted from extracting the parameter signatures to generating the Jacobian matrix.

- *Number of parameters*: If one considers the parameter signatures as sets, then the union of these sets is bound by the number of pixels included in the time-scale plane. As such, the larger the number of parameters (parameter signatures), the higher the competition for pixels. In this paper, we restricted each time series to 128 data points and the transformation to 72 scales, resulting in a time-scale plane of 128 $\times$ 72 dimension. This number of pixels can be distributed among a large number of parameter signatures, certainly more than those ordinarily considered for dynamic systems. Nevertheless, further analysis is warranted to verify this assertion and to establish the range of parameters that are manageable by PARSIM.

- *Selection of the best suite of CWTs*: The results presented in this paper are based on the Gaussian family of CWTs. Depending on the application platform, different combinations of Gauss and Sombrero CWTs and Gaussian smoothing were selected. However, these combinations were selected by trial and error, and not autonomously according to the information content each transformation contributed to the parameter estimation solution. Therefore, devising a measure for identifying the optimal set of CWTs for each application platform will be an interesting problem to solve. Another interesting problem would involve the inclusion of other CWTs in the operation of PARSIM.

- *Range of dominance factors*: Among the various degrees of freedom of PARSIM, the dominance factor is the most critical. In its current form, the dominance factor is selected among a set of dominance factors. A different strategy would entail determining the maximum dominance factor by minimizing the number of zero-valued entropies.

- *Number of edge-point pixels*: The results produced in this paper are based on an arbitrary maximum number of edge point pixels. Given that the number of pixels

included in each parameter signature can have a significant impact on the quality of parameter estimates, identifying a measure whereby the optimum number of edge points can be determined is a potentially worthy topic of study.

CHAPTER 5

CONCLUSION

Two methods of health monitioring were introduced in this dissertation, a direct method and it's complementary inverse method. Both methods leverage the added degrees of freedom inherent in the time-scale domain, such as shape comparison, to advantage. The direct method of fault diagnosis is introduced for isolation of degraded engine components, DSIM, which is ideally suited to in-flight application due to its relatively low computation demand. It identifies the residuals that stand out relative to others in representing engine abnormality and then associates these residuals with the engine components through the health parameters. The results show that DSIM provides adequate repeatability to be used for continual monitoring of component degradation in aircraft engines. The inverse method of health parameter quantification was introduced to assess the severity of the degradation identified by the direct method. This method utilizes the transparencies and degrees of freedom, such as shape attributes, available in the time-scale domain to refine and assess the quality of the data available for parameter estimation. Estimation results from the three test platforms used in this research show PARSIM to be potentially more robust when faced with local minima and shallow gradients as compared to NLS. However, one pitfall which was identified was that if the output sensitivities lack unique and distinguishing shapes, as in the case of the jet engine, PARSIM is rendered less effective in estimating the health parameters.

BIBLIOGRAPHY

[1] Astrom, K., and Eykhoff. System identification - a survey. *Automatica 7* (1971), 123–162.

[2] Chipman, H. A., Kolaczyk E. D. McCulloch R. E. Adaptive bayesian wavelet shrinkage. *J. of the American Statistical Association 92* (1997), 1413–1421.

[3] Danai, K., and McCusker, J. R. Parameter estimation by parameter signature isolation in the time-scale domain. *ASME Journal of Dynamic Systems, Measurement and Control 131* (2009).

[4] Doel, D. L. An assessment of weighted-least-squares-based gas path analysis. *ASME J. of Eng. for Gas Turbines and Power 116* (1994), 366–373.

[5] Doel, D. L. Temper - a gas-path analysis tool for commercial jet engines. *ASME J. of Eng. for Gas Turbines and Power 116*, 1 (1994), 82–89.

[6] Donoho, D. L., and Johnstone, I. M. Adapting to unknown smoothness via wavelet shrinkage. *J. of the American Statistical Association 90*, 432 (1995), 1200–1224.

[7] Espana, M. D., and Gilyard, G. B. Estimation algorithm used in adaptive performance optimization of turbofan engines. *NASA TM 4551* (1993).

[8] et al., A. J. Volponi. Development of an information fusion system for engine diagnostics and health management. *NASA/TM – 2004-212924, Army Research Laboratory Report: ARL-TR-3127* (2004).

[9] et al., I. Kobayashi. Application of a constant gain extended kalman filter for in-flight estimation of aircraft engine performance parameters. *Army Research Laboratory Report: ARL-TR-2955* (2005).

[10] et al., K. Mathioudakis. Turbofan performance deterioration tracking using nonlinear models and optimization techqniques. *ASME J. of Turbomachinery 124* (2002), 580–587.

[11] et al., L. Kerr. Real- time estimation of gas turbine engine damage using a control based kalman filter algorithm. *ASME Paper 91-GT-216* (1991).

[12] et al., S. Fuhrman. The application of shannon entropy in the indentification of putative drug targets. *Elsevier: Journal of Bio Systems 55* (2000), 5–14.

[13] et al., T. Brotherton. estorm: Enhanced self tuning on-board real-time engine model. *Proceedings of the 2003 IEEE Aerospace Conference* (2003).

[14] Fletcher, R. In *Practical Methods of Optimization, 2nd Ed* (1987), Wiley.

[15] Goldberg, D. E. In *Genetic Algorithms* (1989), Addison Wesley.

[16] Gupta S., Ray A., Sarkar S., and Yasar, M. Fault detection and isolation in aircraft gas turbine engines. part 1: Underlying concept. *Proc. of Institute of Mechanical Engineers, Part G: J. of Aeropace Engineering 22*, 10 (2008).

[17] Gupta S., Ray A., Sarkar S., and Yasar, M. Fault detection and isolation in aircraft gas turbine engines. part 2: Validation on a simulation test bed. *Proc. of Institute of Mechanical Engineers, Part G: J. of Aeropace Engineering 222*, 10 (2008).

[18] Ioannou, P. A., and Sun, J. *Robust Adaptive Control*. Prentice Hall, 1996.

[19] Kennedy, M. P. Abc - adventures in bifurication & chaos: A program for studying chaos. *J. Franklin Inst. 331* (1994).

[20] Ljung, L. *System Identification: Theory for the User*, 2nd ed. Prentice Hall, 1999.

[21] Luppold, R. H. Estimating in-flight engine performance variations using kalman filter concepts. *AIAA Paper AIAA-89-2584* (1989).

[22] Mallat, S. *A Wavelet Tour of Signal Processing*, 2nd ed. Academic Press, San Diego, 1998.

[23] Mallat, S. In *A Wavelet Tour of Signal Processing, 2nd Ed.* (1999), Academic Press.

[24] Mallat, S., and Hwang, W.L. Singularity detection and processing with wavelets. *IEEE Trans. on Information Theory 38*, 2 (1992), 617–643.

[25] McCusker, J.R., Currier T., and Danai, K. Improved parameter estimation by noise compensation in the time-scale domain. In *Proc. Of 2009 Dynamic Systems and Control Conference* (Hollywood, California, Oct. 2009), ASME.

[26] McCusker, J. R., and Danai, K. Measurement selection for engine transients by parameter signatures. *ASME Journal of Engineering for Gas Turbines and Power 132* (2010).

[27] McCusker, J. R., Danai, K., and Kazmer, D. O. Validation of dynamic models in the time-scale domain. *ASME Journal of Dynamic Systems, Measurement and Control 132* (2010).

[28] Merrington, G. L. Fault diagnosis of gas turbine engines from transient data. *ASME J. of Eng. for Gas Turbine and Power 111* (1989), 237–243.

[29] Merrington, G. L. Fault diagnosis in gas turbine using a model-based technique. *ASME J. of Eng. for Gas Turbine and Power 116* (1994), 374–380.

[30] Narendra, K. S., and Annaswamy, A. M. In *Stable Adaptive Systems* (1989), Prentice Hall.

[31] Rubinstein, R. Y. In *Monte Carlo Optimization, Simulation, and Sensitivity of Queueing Networks* (1986), Wiley.

[32] Sastry, S., and Bodson, M. In *Adaptive Control* (1989), Prentice Hall.

[33] Seber, G. A. F., and Wild. In *Nonlinear Regression* (1989), John Wiley and Sons, Inc.

[34] Simmons, J. C., and Danai, K. In-flight isolation of degraded engine components by shape comparison of transient outputs. *ASME J. of Eng. for Gas Turbines and Power 134*, 6 (June 2012).

[35] Urban, L. A., and Volponi, A. J. Mathematical methods of relative engine performance diagnostics. *SAE Transactions, Journal of Aerospace 101* (1992), 2025–2050.

[36] Volponi, A. J., DePold, H., Ganguli, R., and Daguang, C. The use of kalman filter and neural network methodologies in gas turbine performance diagnostics: A comparative study. *ASME J. of Eng. for Gas Turbines and Power 125* (2003).

[37] Wang, N., Dayawansa W. P., and Martin, C. F. Van der pol oscillator networks. In *Proc. of the 38th Conference on Decision and Control* (Phoenix, Arizona, USA, 1999).